

Low-frequency spectra of neutron star + OB supergiant binaries: *Does wind density drive persistent and flaring modes of accretion?*

J. van den Eijnden^{1,2*} L. Sidoli,³ M. Diaz Trigo,⁴ I. El Mellah,^{5,6} V. Sguera,⁷ N. Degenaar,¹ F. Fürst,⁸
V. Grinberg,⁹ P. Kretschmar,¹⁰ S. Martínez-Núñez,¹¹ J. C. A. Miller-Jones,¹² K. Postnov,^{13,14} T. D. Russell¹⁵

¹Anton Pannekoek Institute for Astronomy, Universiteit van Amsterdam, Science Park 904, 1098, XH, Amsterdam, The Netherlands

²Department of Physics, University of Warwick, Coventry CV4 7AL, UK

³INAF, Istituto di Astrofisica Spaziale e Fisica Cosmica, Via A. Corti 12, 20133, Milano, Italy

⁴ESO, Karl-Schwarzschild-Strasse 2, 85748, Garching bei München, Germany

⁵Departamento de Física, Universidad de Santiago de Chile, Av. Victor Jara 3659, Santiago, Chile

⁶Center for Interdisciplinary Research in Astrophysics and Space Exploration (CIRAS), USACH, Chile

⁷INAF, Osservatorio di Astrofisica e Scienza dello Spazio, Via P. Gobetti 101, I-40129, Bologna, Italy

⁸Quasar Science Resources SL for ESA, European Space Astronomy Centre (ESAC), Science Operations Departement, 28692, Villanueva de la Cañada, Madrid, Spain

⁹European Space Agency (ESA), European Space Research and Technology Centre (ESTEC), Keplerlaan 1, 2201 AZ, Noordwijk, The Netherlands

¹⁰European Space Agency (ESA), European Space Astronomy Centre (ESAC), Camino Bajo del Castillo s/n, 28692, Villanueva de la Cañada, Madrid, Spain

¹¹Instituto de Física de Cantabria (CSIC-Universidad de Cantabria), 39005, Santander, Spain

¹²International Centre for Radio Astronomy Research, Curtin University, GPO Box U1987, Perth, WA 6845, Australia

¹³M.V. Lomonosov Moscow State University, Sternberg Astronomical Institute, 13, Universitetskij pr., 119234, Moscow, Russia

¹⁴Kazan Federal University, Kremlevskaya 18, 420008 Kazan, Russia

¹⁵Istituto di Astrofisica Spaziale e Fisica Cosmica, INAF, Via U. La Malfa 153, Palermo, I-90146, Italy

Accepted XXX. Received YYY; in original form ZZZ

ABSTRACT

Neutron star high-mass X-ray binaries, where the compact object orbits a massive star in a sufficiently tight orbit to allow accretion to occur, are well-studied in wavebands between the infrared and hard X-rays. Their low-frequency millimeter and radio properties, on the other hand, remain poorly understood. In this paper, we present the first work in a series focusing on the millimeter and radio emission of systems where a neutron star accretes from an OB supergiant. We report ALMA and NOEMA millimeter observations of twelve systems, supplemented by VLA radio observations of six of those targets. Our targets include six Supergiant X-ray Binaries (SgXBs), four Supergiant Fast X-ray Transients (SFXTs), and two intermediate systems. Nine out of twelve targets, including all SFXTs, are detected in at least one millimeter band, while in the radio, only two targets are detected. All detected targets display inverted radio/millimeter spectra, with spectral indices in the range $\alpha = 0.6 - 0.8$ for those systems where accurate SED fits could be performed. We conclude, firstly, that the low-frequency SEDs of neutron star SFXTs and SgXBs are dominated by free-free emission from the OB supergiant’s stellar wind, and that jet emission is unlikely to be observed unless the systems can be detected at sub-GHz frequencies. Secondly, we find that SFXTs are fainter at 100 GHz than prototypical SgXBs, probably due to systematically less dense winds in the former, as supported further by the differences in their fluorescence Fe K α lines. We furthermore compare the stellar wind constraints obtained from our millimeter observations with those from IR/optical/UV studies and bow shock detections, and present evidence for long-term stellar wind variability visible in the thermal emission.

Key words: stars: massive – stars: mass-loss – stars: winds, outflows – stars: neutron – X-rays: binaries – radio continuum: stars

1 INTRODUCTION

Massive stars ($M \gtrsim 8M_{\odot}$) play a central role in a wide range of astrophysical processes. As the rare, high end of the stellar mass scale, massive stars are key in understanding stellar formation and evolution. Given their prevalence to reside in binary or higher-order systems (Sana et al. 2012), massive stars drive binary evolution towards its energetic intermediate (X-ray binaries) and end states (mergers

of binary compact objects). The endpoints of massive star evolution power a range of cataclysmic transients, such as supernovae and long gamma-ray bursts that may lead to the formation of stellar-mass black holes and neutron stars, and kilo-novae in the case of binary neutron star mergers (Eldridge & Tout 2004; Belczynski et al. 2010).

Evolved massive stars drive powerful radiative and mechanical feedback on a range of scales, from their directly surrounding interstellar medium (ISM) to their host galaxies. Their mechanical feedback takes the form of stellar winds, that play a role in many of the earlier mentioned processes – affecting massive star evolution up

* a.j.vandeneijnden@uva.nl

to the transients they power, the evolution of the binaries that host them, or the mass distribution of resulting neutron stars and black holes (Laplace et al. 2025). These winds shape and energize the surrounding ISM, powering particle acceleration in local shocks around individual stars (e.g., del Valle & Romero 2012; del Palacio et al. 2018). On scales of young stellar clusters, stellar winds can combine into a cluster wind to create collective feedback structures in the surrounding medium – where it may power the (re-)acceleration of cosmic rays, as suggested by recent γ -ray detections of such clusters (e.g., Aharonian et al. 2019; Peron et al. 2024; Aharonian et al. 2024) and acceleration modeling (Härer et al. 2023; Vieu & Reville 2023; Menchiari et al. 2025). Moving up further in scale, massive stars and their winds contribute to the heating and structure of their host galaxy (Andersson et al. 2020).

An observational understanding of both the global wind properties and its micro-structure are indispensable to understand this range of feedback and interaction processes. Within the wind, its density structure (where inhomogeneities are often referred to as clumping) and velocity profile affect, for instance, the accretion of the wind by a companion (e.g., Bozzo et al. 2016; El Mellah et al. 2018; Bozzo et al. 2021; Ramachandran et al. 2025). On larger scales, the global mass-loss rate \dot{M}_w and terminal velocity v_∞ of the stellar wind set the power budget for the feedback on – and particle acceleration in – the ISM and stellar cluster surroundings.

A wide range of methods exists to measure the global and micro wind properties (see e.g., Puls et al. 2008; Vink 2022, for reviews). The overall mass-loss rate and velocity profile, for instance, can be studied via P-Cygni profiles in the UV or via the $H\alpha$ recombination line, asymmetry in X-ray emission lines, or the distance between the star and the bow shock it drives in the ISM when moving at supersonic speeds. All but the latter of these methods are affected by the clumping of the winds, as the inferred mass-loss rates depend non-linearly on density (e.g. Hamann & Koesterke 1998; Puls et al. 2006, 2008; Sundqvist & Owocki 2013). When not taken into account, clumping may therefore lead to discrepancies between inferences from different methods (Fullerton et al. 2006). Variability in the wind, combined with non-simultaneous measurements, may further exacerbate such differences (Haucke et al. 2018; Massa et al. 2024). The bow shock method does not suffer from such effects – clumping has smoothed out at these parsec-scale distances from the star and the shock’s radiative time scales far exceed the relevant variability time scales (Mohamed et al. 2012). However, it remains limited in its application due to the required knowledge about the ISM density and temperature (Wilkin 1996; Martinez et al. 2023), and its need for supersonic peculiar motion.

On large scales within the wind, where it has reached its terminal velocity, free-free (Bremsstrahlung) thermal emission dominates the wind’s spectral energy distribution (SED) at radio and (sub-)millimeter wavelengths. As clumping is expected to decrease as a function of radius, this low-frequency continuum emission is expected to be least affected by small-scale density structures (Lamers & Waters 1984; Daley-Yates et al. 2016; Rubio-Díez et al. 2022). For a smooth wind, it was analytically derived in independent papers that this process should lead to a power-law low-frequency spectrum with a slope close to $\alpha = 0.6$ (Wright & Barlow 1975; Panagia & Felli 1975), where the flux density S_ν scales with frequency ν as $S_\nu \propto \nu^\alpha$. Any residual clumping in the outer wind is expected to affect the spectrum’s flux density scaling by maximally 50% in the millimeter band and to a lesser extent at radio wavelengths (Daley-Yates et al. 2016).

In addition to clumping, stellar winds from early-type OB-stars can be noticeably magnetized. Indeed, the surface dipole magnetic field

in about 10% of OBA-stars may reach kG values (Grunhut et al. 2017; Shultz et al. 2019). The magnetized stellar winds can significantly affect the particle acceleration in wind collision zones in gamma-ray binaries with pulsars (Bykov et al. 2024) and be responsible for triggering of SFXT outbursts by magnetic reconnection near neutron star magnetospheres (Shakura et al. 2014a).

Low-frequency observations of massive star winds have predominantly been performed before the current generation of radio and millimeter interferometers (e.g., Bieging et al. 1989; Leitherer & Robert 1991; Leitherer et al. 1995; Blomme et al. 2003; Benaglia et al. 2007; Benaglia & Koribalski 2007) with typical detection limits of hundreds of μ Jy to several mJy. Current instrumentation is capable of significantly deeper observations: in radio, such instruments include the upgraded Karl G. Jansky Very Large Array (VLA), the upgraded Australia Telescope Compact Array (ATCA), and Square Kilometer Array (SKA) precursors such as MeerKAT and the Australian SKA Pathfinder (ASKAP). In the (sub-)millimeter band, the current state of the art is provided by the Northern Extended Millimeter Array (NOEMA) and the Atacama Large Millimeter/submillimeter Array (ALMA). Fenech et al. (2018), Andrews et al. (2019), and Gallego-Calvente et al. (2021) have recently showcased the power of combining VLA and ATCA radio with ALMA millimeter observations of Westerlund 1 and the Arches cluster to study their massive stellar population. However, as studies at the enhanced sensitivity of these instruments remain rare, new applications of the low-frequency approach to understand global stellar wind characteristics is warranted (Vink 2022).

1.1 Probing massive star winds with millimeter, radio, and X-ray observations of accreting neutron star binaries

When massive stars reside in a binary system with a compact object companion, the interaction between the stellar wind and the compact object can provide an orthogonal view on the wind’s global and small-scale structure. The nature of the compact object in these binaries is most often a neutron star. Young, energetic neutron stars that still launch a powerful pulsar wind are thought to power a subset of so-called γ -ray binaries, whose broad-band SED is dominated by the non-thermal shock between stellar and pulsar wind (e.g. Dubus 2013). More commonly, the closely-orbiting neutron star spins slowly ($\gtrsim 1$ second period) and does not launch a pulsar wind (Reig 2011; van den Eijnden & Rajwade 2024). As a result, the interaction with the massive star instead takes the form of accretion, as the neutron star gravitationally captures the stellar wind, in systems named High-Mass X-ray Binaries (HMXBs). This accretion process results in X-ray emission, whose luminosity can provide an independent constraint on the stellar wind properties, especially if information about the orbit is known. Alternatively, varying X-ray absorption along the binary can reveal the overall density structure, as well as clumpiness, of the stellar wind (Grinberg et al. 2015; El Mellah et al. 2020; Diez et al. 2022). Low-frequency observations of the thermal stellar wind emission trace the wind far beyond typical binary separation (Güdel 2002); stellar wind accretion by the neutron star, on the other hand, probes the wind’s inner regions. For eccentric orbits, furthermore, different wind regions are sampled as the neutron star moves towards and away from the star. All combined, the radio, millimeter, and X-ray properties of the HMXB along its orbit provide complementary views of the wind’s global and micro-structure.

While the presence of a neutron star companion provides an orthogonal probe of the stellar wind, it also complicates the system in two manners: the launch of relativistic jets affecting the low-frequency methods and the introduction of intrinsically complex

accretion behavior affecting the X-ray methods. The effect of jets is seen most clearly in the black hole – massive star binary Cyg X-1, where the jet dominates at radio and millimeter frequencies over the stellar wind’s large-scale emission and strongly dynamically interacts with the stellar wind (Fender et al. 2000; Zdziarski 2012; Miller-Jones et al. 2021). The radio jets of slowly-spinning neutron stars are observed to be significantly weaker than in Cyg X-1 (van den Eijnden et al. 2018, 2021), but their interaction with stellar winds may brighten them (van den Eijnden et al. 2024). Therefore, the potential contribution of such jets to the low-frequency emission of neutron star HMXBs should be taken into account. In a similar fashion, other non-thermal processes – the interaction of clumps with large-scale wind structures induced by the orbiting neutron star – may contribute at low frequencies, although such interactions have not been observed directly in HMXBs yet (van den Eijnden et al. 2021).

The complex accretion behavior complicates any inferences about the stellar wind made from X-ray observations. In this context, the different modes of accretion seen for neutron stars orbiting OB supergiants are particularly noteworthy. HMXBs hosting OB supergiants show an apparent dichotomy in X-ray behavior: the Supergiant X-ray Binaries (SgXBs) that accrete persistently on one hand, and the Supergiant Fast X-ray Transients (SFXTs) that accrete in a transient, flaring manner on the other. The origin of this difference in X-ray behavior is poorly understood, but may be driven by the properties of the neutron star (e.g., Shakura et al. 2012, 2014b), donor star and its stellar wind (Negueruela 2019; Giménez-García et al. 2016; Hainich et al. 2020), binary orbit, or complex combinations of the above (see e.g., Sidoli 2017; Kretschmar et al. 2019, for recent reviews). While the difference between the accretion in SFXTs and SgXBs complicates using the X-ray observations as a probe of the wind, the argument can be turned around: better understanding the winds, for instance via low-frequency observations, can also test the role of the wind properties in driving accretion modes.

Published low-frequency constraints on neutron star HMXBs, particularly SFXTs, remain sparse. van den Eijnden et al. (2021) presented ATCA radio observations of eleven SgXBs, detecting emission from five systems. These radio-band-only observations, however, did not unambiguously reveal the origin of the emission beyond doubt: stellar winds only, accretion-driven jets, other non-thermal processes, their interaction, or their superposition, all remained consistent with the observations. Millimeter observations, where the stellar wind is more likely to dominate due to its strongly inverted spectrum, are therefore crucial. A pilot NOEMA millimeter study of one SgXB and one SFXT was published by van den Eijnden et al. (2023), reporting the SFXT as the first millimeter-detected neutron star accreting from a massive star. With just one source per neutron star HMXB sub-class, however, this pilot study could not yet reveal whether systematic low-frequency differences between SFXTs and SgXBs may be linked to their different accretion modes.

1.2 Constructing a first sample of neutron star HMXBs observed at millimeter frequencies

Here, we present the first extended sample of neutron stars accreting from massive stars, observed at millimeter and radio wavelengths. Our campaign performed millimeter observations with ALMA and NOEMA, supplemented by a supporting VLA radio campaign and X-ray observations using *Swift*, *MAXI*, and *INTEGRAL*. In this first paper, we focus on an overview of the target sample and the low-frequency observations, presenting the detection of nine out of twelve targets at millimeter wavelengths. We then specifically discuss the

dominant origin of the low-frequency emission, comparing stellar wind and relativistic jet scenarios. We subsequently discuss whether the low-frequency spectra of neutron star HMXBs contain evidence that stellar wind properties drive the difference between SFXTs and SgXBs. Finally, we briefly compare the low-frequency wind inferences with bow shock inferences for two targets, and discuss wind variability in the context of our observations. In a follow-up paper, we will focus on more detailed modelling of the wind and the accretion process in our targets, combining the low-frequency data presented in this paper with X-ray constraints and updated modelling of the stellar wind’s thermal free-free emission.

2 TARGETS, OBSERVATIONS, AND DATA ANALYSIS

2.1 Targets

In this work, we discuss the twelve targets that have been observed at the current state-of-the-art millimeter band sensitivity (e.g., RMS sensitivities of 10–40 μ Jy/bm). Our target sample is summarized in Table 1, where we list the source name, type (SgXB, SFXT, or intermediate, i.e., showing signatures of both classes), the observatories used for the millimeter, radio, and X-ray observations, and the distance and donor type with references. The NOEMA millimeter observations of two targets (the SFXT IGR J18410-0535 and SgXB X1908+075) were already published in the pilot study by van den Eijnden et al. (2023) and are included again here. For the former system, new millimeter observations with ALMA are presented here for the first time. The full sample spans a range in accretion behaviour and donor star type, but has primarily been constructed based on observability with NOEMA / ALMA and distance. For seven targets, we list only the *Gaia* DR3 distance, providing the best constraint. For four targets, other works using (a combination of) different methods provide a better constrained distance measurement than *Gaia*, which we adopt instead.

For IGR J18410-0535, we list a range in distance estimates, as this property is poorly constrained (see Van den Eijnden et al. 2023, for the impact this has on further understanding of its millimeter emission). For 4U 2206+54, we list HMXB as binary type, as its donor is not a supergiant but a O9.5V star (Blay et al. 2006). In our Figures, we group it with the SgXB as it persistently accretes from the donor star’s wind. However, we will note its different nature wherever relevant. Finally, we note that 4U 1907+09 is listed as SgXB, but shows signatures of SFXTs-like X-ray dipping and has therefore been discussed as a source in-between both classes as well (Doroshenko et al. 2012).

2.2 Millimeter observations

2.2.1 NOEMA observations

Six targets, including one overlapping with the ALMA targets (4U 1907+09), were newly observed with NOEMA in a single-band detection experiment at 100 GHz. The observing program (number w23bo) consisted of four tracks, with one or two targets per track; two targets were combined in a single track if their proximity allowed the use of shared calibrators to optimize overheads. Each track was observed across multiple dates to achieve the required sensitivity. The exact dates per target are listed in Table 2. The observations were performed in a continuum-only point-source-detection setup, where the observing band is split into a Lower Side Band (LSB; 82.5–90 GHz) and Upper Side Band (USB; 98–105.5 GHz) with centers separated by 15.488 GHz. All observations consisted of a standard

Table 1. The target sample, listed target name, type, observatory per band, distance, and donor star type, the latter two with references. *Already published in [van den Eijnden et al. \(2023\)](#). **Range represents the range in best-fit measurements reported by the listed references. ***While not a SgXB according to its donor classification, we will group it amongst the SgXB class due to its persistent X-ray properties akin to the other SgXBs.

Name	Type	MM	Radio	Distance [kpc]	Distance refs	Donor type	Donor type refs
4U 1700-37	SgXB	ALMA	VLA	1.58 ± 0.07	van der Meij et al. (2021)	O6.5 Iaf+	Walborn (1990)
Vela X-1	SgXB	ALMA	VLA	$1.99^{+0.13}_{-0.11}$	Kretschmar et al. (2021)	B0.2 Ia	Same as distance ref
4U 1907+09	SgXB	ALMA	VLA	3.6 ± 0.7	Gaia DR3	O8/O9 Ia	van Kerkwijk et al. (1989)
		NOEMA					
X1908+075	SgXB	NOEMA*	–	4.58 ± 0.50	Martínez-Núñez et al. (2015)	B0-B3	Same as distance ref
2S 0114+650	SgXB	NOEMA	–	4.5 ± 0.2	Gaia DR3	B1Ia	Reig et al. (1996)
4U 2206+54	HMXB***	NOEMA	–	3.1 ± 0.1	Gaia DR3	O9.5V	Blay et al. (2006)
IGR J00370+6122	Interm.	NOEMA	–	3.4 ± 0.2	Gaia DR3	B1 Ib	González-Galán (2014)
IGR J19140+0951	Interm.	NOEMA	–	4.0 ± 1.7	Gaia DR3	B0.5 Ia	Torrejón et al. (2010a)
IGR J17544-2619	SFXT	ALMA	VLA	2.52 ± 0.17	Gaia DR3	O9I	Giménez-García et al. (2016)
IGR J18410-0535	SFXT	ALMA	VLA	$3.2\text{--}13.9^{**}$	Sguera et al. (2009)	B1Ib	Same as distance refs
		NOEMA*	ATCA*		Nespoli et al. (2008)	B1I	
					Negueruela et al. (2008)	B0.2Ibp	
					Coleiro & Chaty (2013)		
					Gaia DR3		
SAX J1818.6-1703	SFXT	ALMA	VLA	2.1 ± 0.1	Torrejón et al. (2010a)	B0.5Iab	Same as distance ref
IGR J18483-0311	SFXT	NOEMA	–	$2.7^{+1.5}_{-0.8}$	Gaia DR3	B0.5-B1	Torrejón et al. (2010a)

Table 2. The results of the NOEMA and ALMA millimeter observations. Uncertainties in flux density are given at 1σ , upper limits at 3σ . Observations listed at 40, 150, and 300 GHz were performed by ALMA. Observations at 100 GHz were performed by NOEMA. For the ALMA observations, we list the start time of the first target scan in the second column. For the NOEMA observations, we list the multiple dates on which observations for that target were performed. T_{obs} is the total observing time, including overheads, per band, in minutes. *ALMA observations are separated by at least one orbital period. **NOEMA observations are separated by at least one orbital period. ***The ALMA and NOEMA observation sequences both, individually, fall within a single orbital period, but the two telescope campaigns are separated by more than an orbit.

Name	Date(s)/time(s)	T_{obs} [min]	ν [GHz]	F_{ν} [μJy]	L_{ν} [erg/s/Hz]
4U 1700-37*	2024-10-05 20:57:02	30	40	1417 ± 12	$(4.2 \pm 0.4) \times 10^{18}$
	2024-10-19 22:54:44	25	150	3729 ± 21	$(11.1 \pm 1.0) \times 10^{18}$
	2024-10-01 21:34:03	38	300	5508 ± 28	$(16.5 \pm 1.5) \times 10^{18}$
Vela X-1	2024-10-05 11:42:35	29	40	375 ± 12	$(1.8 \pm 0.2) \times 10^{18}$
	2024-10-05 12:31:45	24	150	994 ± 22	$(4.7 \pm 0.6) \times 10^{18}$
	2024-10-04 12:30:04	37	300	1775 ± 30	$(8.4 \pm 1.1) \times 10^{18}$
4U 1907+09**	2024-11-04 22:14:56	24	40	40 ± 19	$(6.2 \pm 3.8) \times 10^{17}$
	2024-10-06 23:38:27	27	150	113 ± 39	$(1.8 \pm 0.9) \times 10^{18}$
	2024-10-01 22:13:27	42	300	–	–
X1908+075**	2024-02-24/28, 2024-03-14	150	100	57 ± 13	$(8.8 \pm 4.0) \times 10^{17}$
	2023-01-25, 2023-02-07	88	100	< 34.4	$< 8.6 \times 10^{17}$
	2024-01-14, 2024-01-16	216	100	63 ± 11	$(1.5 \pm 0.3) \times 10^{18}$
4U 2206+54	2024-03-11/19	108	100	< 36	$< 4.1 \times 10^{17}$
IGR J00370+6122	2024-01-14, 2024-01-16	216	100	< 33	$< 4.6 \times 10^{17}$
IGR J19140+0951**	2024-02-02/4/28, 2024-03-14	126	100	209 ± 12	$(4.0 \pm 3.4) \times 10^{18}$
IGR J17544-2619*	2024-10-05 23:23:15	38	40	< 34	$< 2.6 \times 10^{17}$
	2024-10-19 23:20:18	68	150	108 ± 12	$(8.2 \pm 1.4) \times 10^{17}$
	2024-10-11 19:46:19	61	300	108 ± 13	$(8.2 \pm 1.5) \times 10^{17}$
IGR J18410-0535***	2024-10-05 22:03:54	38	40	< 38	$< 2.1 \times 10^{18}$
	2024-10-07 00:33:24	65	150	40 ± 11	$(2.3 \pm 1.3) \times 10^{18}$
	2024-10-01 22:55:08	63	300	86 ± 15	$(4.9 \pm 2.6) \times 10^{18}$
SAX J1818.6-1703	2023-02-20/22/23	88	100	63.4 ± 9.6	$(3.6 \pm 1.9) \times 10^{18}$
	2024-10-06 21:11:21	37	40	123 ± 14	$(6.5 \pm 0.8) \times 10^{17}$
	2024-10-06 22:31:27	65	150	288 ± 12	$(1.5 \pm 0.1) \times 10^{18}$
IGR J18483-0311**	2024-10-02 01:21:33	61	300	463 ± 17	$(2.4 \pm 0.1) \times 10^{18}$
	2024-03-20, 2024-07-11/12	462	100	112 ± 9	$(9.7 \pm 5.8) \times 10^{17}$

Table 3. Summary of the VLA radio observations of the six ALMA targets. The date/time column refers to the start of the observation. Each observation lasted 1 hour including overheads. The third and fourth column report the flux and phase calibrator sources (the same at each frequency). Robust refers to the robustness parameter in the CASA TCLEAN task. Errors on the flux density are quoted at 1σ , upper limits are quoted at 3σ . *Note that the 10-GHz observation of 4U 1700-37 suffered from gain calibration issues; this flux density is therefore not used in further analysis or interpretation.

Name	Date / time [UTC]	Flux calibrator.	Phase calibrator	Frequency [GHz]	Robust	Flux density [μ Jy]
4U 1700-37	2024-10-15 21:01:00	3C286	J0922-3959	6	1	264 ± 11
				10	1	$207 \pm 87^*$
Vela X-1	2024-10-17 13:04:00	3C286	J1717-3948	6	1	73.7 ± 10.0
				10	1	91.0 ± 15.0
4U 1907+09	2024-10-16 01:46:00	3C48	J1912+0518	6	1	< 24
				10	1	< 36
IGR J17544-2619	2024-10-17 01:05:00	3C48	J1825-0737	6	0.5	< 30.0
				10	0	< 60.0
IGR J18410-0535	2024-10-17 02:05:00	3C48	J1751-2524	6	–	–
				10	0	< 78.0
SAX J1818.6-1703	2024-10-19 22:45:00	3C286	J1825-1718	6	1	< 27
				10	1	< 100.0

scan setup, with multiple calibrators used for bandpass, amplitude, and phase calibration; the latter two were performed with one or multiple calibrators interleaving the target scans.

We calibrated the data using the CONTINUUM AND LINE INTERFEROMETRIC CALIBRATION (CLIC) software within the GILDAS package (version Jan 2025), designed specifically for the analysis of NOEMA observations. The calibration was performed using the standard pipeline, which handles bandpass, phase, and amplitude calibration, as well as automated flagging using the pre-defined limits for detection experiments. The pipeline output was manually inspected and combined with observing log information to prepare and optimize re-runs of the pipeline, until satisfactory calibration was obtained. For observations in A configuration – NOEMA’s most extended configuration, used between 2024 February 28 and March 20 – acceptable calibration required switching from antenna to baseline-based configuration for bandpass and amplitude. Calibration was performed separately per observing date; for the 2024 March 19 observations, the raw data was split into three parts as one antenna dropped out and came back online during the observations. Lacking a bandpass calibrator or sufficient exposure of the other calibrators, the second and third segment could not be adequately calibrated and were therefore dropped from further analysis. Similarly, issues with the bandpass calibration prevented the use of data collected on 2024 March 14. Finally, the calibrated datasets were converted to UV-tables (.UVT format) for further analysis, with one UV-table per target per side band. All pipeline reports, and pipeline logs in plain-text .CLIC format, are available in this paper’s Data Reproduction Package.

We performed cleaning and imaging of the observations using the MAPPING software within GILDAS. For each observation, we first performed the analysis per side band, to assess whether the target was significantly detected in each band, before combining the two UV-tables into a single band. For this analysis, we frequency-averaged the UV-tables using uv_cont and cleaned across a region with size twice the full-width-half-maximum of the primary beam, down to a flux density level of 2 times the expected RMS noise (2.5 times for data including A configuration). After inspecting the resulting image and measuring the RMS noise with the GO NOISE routine, we fitted a point source model in the UV plane with initial position estimated at the phase centre. While the detected targets are all visible in their respective side-band images, we use the UV fit outcome as the formal assessment of detection: for three out of six sources, the fit results in a significant source at the phase centre, while for the two

non-detected sources, a flux density below the RMS noise is found. Finally, for 4U 1907+09, this procedure is performed at a small offset from the phase centre, due to a slight pointing offset, also leading to a target detection. Finally, we merge the side-band UV-tables using uv_merge for a final RMS measurement and flux density measurement for detected sources. In Table 2, we list the detected flux density in the combined 100-GHz band for four detected targets, and the three sigma upper limit for the two non-detected targets.

2.2.2 ALMA observations

An additional six targets were observed with ALMA in a multi-band observing campaign (under code 2024.1.00657.S). The targets, three SgXBs and three SFXTs, were each observed at Bands 1 (40 GHz), 4 (150 GHz), and 7 (300 GHz). The exposure times were set up to optimize sensitivity at the lower frequencies, where an inverted stellar-wind type spectrum is expected to be faintest. All 18 observations were successfully performed between 2024 Oct 01 and Nov 04 and reached the intended RMS sensitivity.

We performed further analysis using the standard ALMA pipeline images for each target and (sub) band. Specifically, we first analysed the primary-beam-corrected continuum image for each full band, making use of self-calibrated images when available (i.e., when the target was sufficiently bright). We converted each FITS image into the .IMAGE format of the Common Astronomy Software Application (CASA v.6.6.5.31) through its IMPORTFITS tool. Those images were subsequently fitted with a 2D Gaussian point source in the image plane, fixing the Gaussian’s shape to the major and minor axes and position angle of the synthesized beam. We measured the RMS noise of each image in an annulus with inner and outer radii of 15 and 30 pixels, respectively, around the phase centre, thereby avoiding target emission. We regard any flux density at least three times the surrounding image RMS as a detection. If the target was detected significantly at this threshold, we repeated this procedure on the four sub-bands of each ALMA band. In all cases, a significant source detection in the full band translated to detections in each of the four sub-bands. All ALMA images and the script to repeat these measurements are included in this paper’s Data Reproduction Package. The results of this ALMA analysis are listed in Table 2.

2.3 Radio observations

As part of the ALMA observing campaign, we observed the six ALMA targets with the VLA and 6 and 10 GHz (Program SA110657). The six observations were taken between 15 and 19 October 2024, while the array was in A configuration, with a maximum of 17 day separation between a target’s VLA epoch and one of its ALMA band observations. Each target was observed for one hour including overheads, resulting in approximately 13 minutes on target per observing band. Both bands were setup with 3-bit samplers to yield 4 GHz of bandwidth per band. Different primary and secondary flux calibrators were chosen per target, depending on the source position and the LST of the observation.

We reduced the observations using *CASA* v.6.6.5.31 (CASA Team et al. 2022) to perform data inspection and flagging, calibration, and imaging following standard practices. Specifically, the data were imaged using *TCLEAN* at both observing frequencies separately, varying the robustness parameter to optimize the trade-off between sensitivity and the effect of side-lobes and imaging artifacts. If a radio counterpart was detected at the known source position, we used *IMFIT* to measure its flux density by fitting a 2D Gaussian with full-width-half-maxima and orientation fixed to the synthesized beam. We calculated the flux density error as the RMS variability across a close-by region devoid of sources. For undetected targets, we calculate the RMS across the source position and report the 3σ upper limit on the flux density. Further details of the observations, including times of observation, optimal robustness parameter, calibrator sources, and flux density limits, are listed in Table 3.

In two cases, observational issues strongly affect the quality of the data to the level where we do not use their results in the further analysis. In the 6-GHz observation of IGR J18410-0535, large side-lobes and artifacts are present in the image, regardless of imaging parameters and whether the flagging and calibration was performed fully manually or started from the VLA pipeline. These artifacts do not resemble those expected from nearby or diffuse sources. In the 10-GHz observation of 4U 1700-37, good phase calibration solutions using the secondary calibrator were challenging to obtain. Improving the calibration by attempting self-calibration on the target, expected at several hundreds of μJy , did not fully resolve these issues. The resulting imaging does reveal a potential source at the target position, but not at 3σ significance due to the high remaining image noise. The potential counterpart is seen at $207 \pm 87 \mu\text{Jy}$, which we list in Table 3 and include in the SEDs, but do not use in further SED fitting or interpreting the broad-band spectrum.

We finally note that we cross-referenced the position of each target in radio survey data from the Very Large Array Sky Survey (Gordon et al. 2021), the MeerKAT Galactic Plane Survey (Goedhart et al. 2024), the Rapid ASKAP Continuum Survey (McConnell et al. 2020), and the ASKAP Evolutionary Map of the Universe (EMU) survey (Norris & the EMU Team 2011). None of these radio surveys returned a counterpart to the considered system, with unconstraining upper limits in comparison to our VLA and ALMA/NOEMA observations.

3 RESULTS

3.1 Millimeter and radio imaging

Using the methods described in the previous Section, we assessed the images and measured the flux densities of all ALMA and NOEMA observations. The measured flux densities or 3σ upper limits are reported in Table 2 and plotted as a function of frequency in Fig-

ure 1. Out of the total sample of twelve sources, nine sources are detected in the millimeter band. The first millimeter-detected SFXT, IGR J18410-0535, was re-detected with ALMA, confirming the earlier NOEMA result. In total, five out of the six ALMA targets are significantly detected in two or three bands at the phase centre (see below). Three out of six NOEMA targets were detected at the phase centre. In Table 2, the results per band are listed; flux densities per sub-band can be found in the Appendix. The Appendix also includes images for all bands and all targets.

It is worth explicitly discussing 4U 1907+09. Due to a slight offset in target coordinates, 4U 1907+09 was not located at the pointing / phase center in both the ALMA and NOEMA observations. This has two important consequences: firstly, it falls just outside the field for the ALMA observation at 300 GHz, where the primary beam is smallest. Secondly, especially for the ALMA observations, the offset from the phase centre increases the local RMS. The two ALMA images covering the position of 4U 1907+09 field (e.g., 40 and 150 GHz) are shown in Figure 2, as is the NOEMA 100-GHz image. For the two ALMA images, we manually measure the flux density at the offset source position, yielding the flux density levels reported in Table 2. The local, enhanced RMS yields formally insignificant detections ($< 3\sigma$) for the 40 and 150 GHz ALMA observations. Yet, we take the presence of a faint point source at the correct position in both ALMA images, as well as the $\geq 4\sigma$ NOEMA detection, as sufficient evidence to claim a source detection. We therefore treat 4U 1907+09 as detected from here on, bringing the total number of detected ALMA targets to six out of six, and detected NOEMA targets to four out of six (considering only newly observed targets from program w23bo). Due to overlap between ALMA and NOEMA targets and including earlier campaigns, nine of twelve total targets are detected in the millimeter band.

For all targets, we use the observed flux density (limit) and distance to calculate the specific luminosity, defined as $L_\nu = 4\pi F_\nu D^2$ and listed in Table 2. Ignoring the exact spectral shape by calculating the specific luminosity allows us to compare all targets among each other and with other low-frequency stellar sources. We calculate its error by propagating both flux density and distance errors, explaining the significant errors for some targets through the squared dependence on sometimes poorly constrained distances¹.

In the ALMA observations, we explored whether any evidence for short-time-scale flaring or narrow emission line features could be seen. These searches were motivated by, respectively, the variability seen in X-rays for both SgXBs and (in particular) SFXTs, and the rest frequency of the H54 α radio recombination line (RRL) at 40.630 GHz. We searched the ALMA observations in each band where the target was detected at $> 3\sigma$ significance (e.g., excluding 4U 1907+09) using the *uvFIT* tool in *CASA* and the calibrated measurement set. We measured the target light curves at both a 10 second and 1 minute time resolution, but did not find evidence for flaring or slower flux variations throughout the observations. The poorer uv-coverage and lower sensitivity of NOEMA prevented us from repeating this approach on the NOEMA data. Comparing, however, the NOEMA flux densities of detected targets between individual observing days revealed potential, low-level variations. We will discuss such longer time-scale variability in Section 4.4. Finally, we found no evidence for an RRL around 40.630 GHz in the ALMA Band 1 pipeline spectrum of any target.

The results of the VLA radio observations of the six ALMA targets

¹ Note that for IGR J18410-0535, we adopt the 6.9 ± 1.7 kpc out of the potential range.

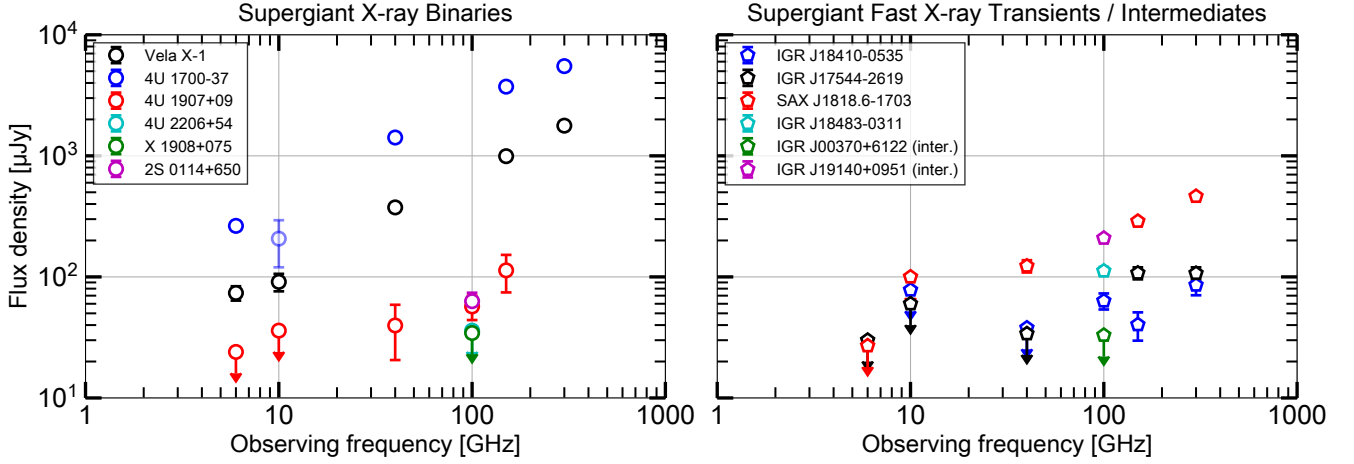


Figure 1. The low-frequency spectral energy distributions of all twelve targets, separated into SgXBs (left) and SFXTs / intermediates (right). For each source, we plot all available ALMA and NOEMA data, including those from Van den Eijnden et al. (2023). We also show the coordinated VLA flux density (limits) for the six ALMA targets. At several frequencies, upper limits overlap; in all those cases (particularly the 6/10 GHz bands in the right-hand panel) the overlapping points all represent upper limits. In the left-hand panel at 100 GHz, above the two overlapping limits, two detections are plotted at overlapping flux density.

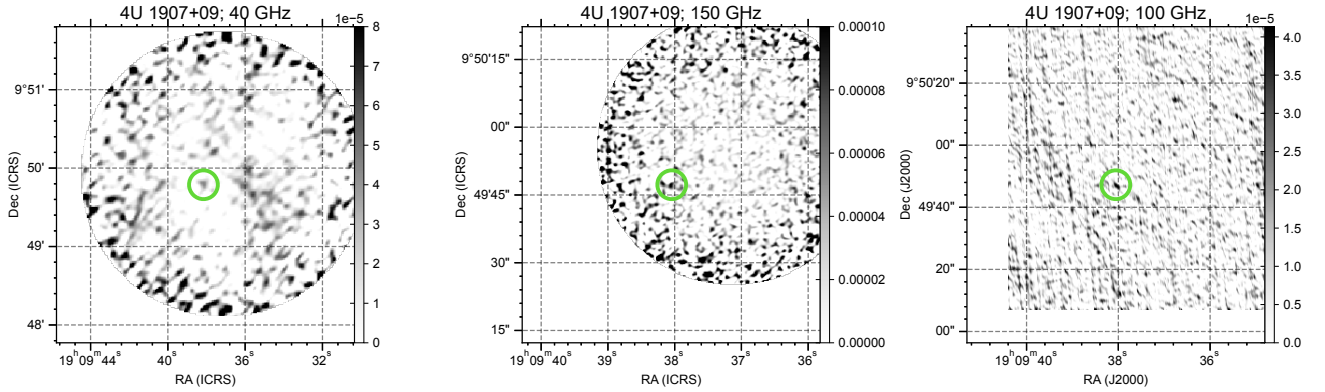


Figure 2. The two ALMA images at 40 GHz (left) and 150 GHz (middle), and the NOEMA image at 100 GHz (right) of the field of 4U 1907+09. The green circle in each panel is centred on the position of the SgXB, which is used as the plotting center of each panel. With increasing frequency, the field of view shrinks, causing the pointing centre to shift to the upper right in the ALMA images. While formally not $> 3\sigma$ significant in both ALMA images, we measure its flux and report it as a detection due to its consistent presence in all images covering the position; in particular, the NOEMA 100-GHz image shows a millimeter counterpart at $\geq 4\sigma$. The ALMA 300-GHz image, where the source position is not covered, is shown in Figure A2.

are summarized in Table 3. Significant radio emission was detected from 4U 1700-37 and Vela X-1, the two SgXBs already detected with ATCA by van den Eijnden et al. (2021). Both sources are detected at lower radio flux densities in our VLA observations, despite the similar observing frequencies to the previous ATCA campaign. The most striking difference is seen for 4U 1700-37, which was detected at approximately twice the flux density by van den Eijnden et al. (2021). The third SgXB, 4U 1907+09, is not detected at radio frequencies, nor are any of the three SFXTs targeted with the VLA. All detected flux densities or 3σ upper limits are plotted in the SEDs of Figure 1. The radio detections and non-detections appear generally unsurprising given the flux densities and spectral shapes of the ALMA targets, coupled with the typical VLA sensitivities: only the two millimeter-brightest systems are detected in radio. While our VLA observations are, to our knowledge, the deepest constraints on SFXT radio emission to date, this source class remains completely radio undetected.

3.2 Low-frequency SED fitting

We attempt to fit the low-frequency millimeter or radio + millimeter SEDs of our targets with a power law model $S_\nu = \xi S_0 (\nu/\nu_0)^\alpha$. For all sources with multiple millimeter band detections (i.e., all ALMA targets), we set $S_0 = 1$ mJy and $\nu_0 = 121.6$ GHz, equal to the mean of the three ALMA centroid frequencies in log space. The choice of model shape reflects the expected power law shape for both a thermal wind (in the regime where the size of the millimeter and radio photosphere exceed the size of the star) and non-thermal jet spectrum. We skip sources with a single-band non-detection (X1908+075, IGR J00370+6122, 4U 2206+54). We note that, for sources with only a single NOEMA band detection, we can use the two NOEMA sub-bands to calculate the spectral index (as the number of bands equals the number of parameters). Here, we find values of $\alpha = -1.2 \pm 2.1$, $\alpha = -1.0 \pm 0.7$, and $\alpha = -0.6 \pm 0.9$ for 2S 0114+650, IGR J19140+0951, and IGR J18483-0311, respectively. Due to the large

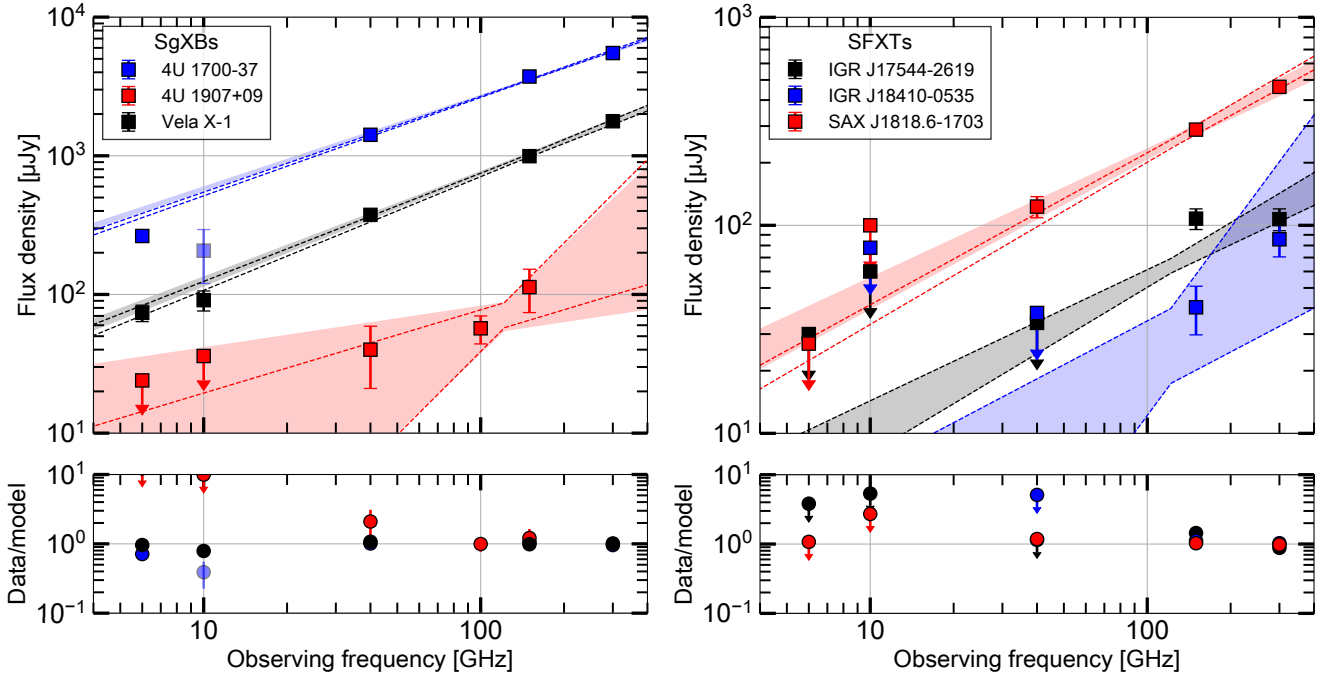


Figure 3. Fits of a power-law radio / millimeter spectrum $S_\nu = \xi S_0(\nu/\nu_0)^\alpha$ to the six ALMA targets. The left and right panels show the three SgXBs and SFXTs, respectively, where we stress the difference in vertical extent. The shaded regions and dashed lines indicate the 1σ confidence regions of the MCMC fits, including only the ALMA data and both the ALMA and VLA data, respectively. Below each spectral fit, the residuals are shown as data divided by model, for the fit to the ALMA and VLA data. Note that we plot the 10-GHz point for 4U 1700-37 but do not use it in the MCMC fit.

uncertainties on these values compared to the fits discussed below and, in particular, the small fractional frequency difference (~ 0.15) between the two sub-bands, we do not use these measurements further in our interpretation of the SED shapes.

For the remaining six (ALMA / VLA) targets, we fit the power law model using an MCMC fitting routine. We take non-detections into account by assigning a zero probability (or, in the fitting routine, a minus infinity log probability) to any model that predicts a flux above a 3σ upper limit. We assume flat priors on the spectral index α and on the logarithm of the normalization parameter, $\log \xi$. We perform three versions of the SED fit: firstly, we fit the ALMA SEDs using the three full ALMA bands, followed by a fit to the ALMA SEDs using the three times four sub-bands as a consistency check. Subsequently, we also fit the ALMA + VLA SEDs, using the full bands (6, 10, 40, 150, and 300 GHz) for each. Finally, for 4U 1907+09, we only perform a single fit to the ALMA 40 and 150 GHz plus the NOEMA 100 GHz data, given the offset pointing and therefore low signal-to-noise. For each fit, we report the resulting parameter estimates and their 16/84th percentile confidence intervals in Table 4. We also plot the 1σ confidence regions of the fitted power law models, for the fits listed in Table 4, alongside the data in Figure 3. Corner plots from all fits can be found in the Data Reproduction Package of this work.

As expected from the SED shown in Figure 1, we find inverted spectral indices for all six targets. Particularly, the lowest spectral index taking into account the 1σ uncertainties is found for 4U 1907+09: $\alpha = 1.0^{+0.9}_{-0.7}$, from the millimeter data only. Regardless of the inclusion or exclusion of radio data, the spectral indices are typically slightly higher than expected in the theoretical Wright & Barlow (1975) and Panagia & Felli (1975) prediction of $\alpha = 0.6$: for the most accurately measured spectral indices, we find values in the approximate range $\alpha \approx 0.6 - 0.8$. Such deviations may be expected in

Table 4. Results of the power law model MCMC fits, $S_\nu = \xi S_0(\nu/\nu_0)^\alpha$, to the six targets with ALMA + VLA data assuming flat priors on spectral index α and on the logarithmic normalization $\log \xi$. The two different fits differ in whether the VLA radio data was included in the fit. Note that for IGR J17544-2619 and IGR J18410-0535, the fit remains the same, as the VLA data are unconstraining compared to the millimeter band. *For 4U 1907+09, the NOEMA 100-GHz band was included instead of the ALMA 300-GHz band.

Target	ALMA full bands		ALMA full bands + VLA	
	$\log \xi$	α	$\log \xi$	α
4U 1700-37	0.489 ± 0.002	0.67 ± 0.01	0.484 ± 0.002	0.70 ± 0.01
Vela X-1	-0.06 ± 0.01	0.78 ± 0.02	-0.07 ± 0.01	0.80 ± 0.02
4U 1907+09*	$-1.15^{+0.09}_{-0.11}$	$1.0^{+0.9}_{-0.7}$	$-1.14^{+0.08}_{-0.10}$	$1.2^{+0.8}_{-0.6}$
IGR J17544-2619	$-1.19^{+0.03}_{-0.04}$	$0.70^{+0.10}_{-0.07}$	$-1.19^{+0.03}_{-0.04}$	$0.70^{+0.10}_{-0.07}$
IGR J18410-0535	$-1.55^{+0.15}_{-0.21}$	$1.2^{+0.6}_{-0.5}$	$-1.55^{+0.15}_{-0.21}$	$1.2^{+0.6}_{-0.5}$
SAX J1818.6-1703	-0.60 ± 0.02	0.67 ± 0.05	-0.62 ± 0.01	$0.75^{+0.03}_{-0.02}$

a thermal stellar wind by relaxing assumptions around its velocity structure and acceleration profile: a wind that is still accelerating at the typical emission radii probed by the radio and millimeter bands will show a spectral index in excess of $\alpha = 0.6$ (see also Erba & Ignace 2022).

Comparing our different fits, we find that only for IGR J17544-2619 and IGR J18410-0535, differences in the fit parameters are found when changing the full ALMA band data to the ALMA sub-bands. In those cases, the two parameters remain poorly constrained in comparison to the full ALMA bands. This change is to be expected: for these two weakest millimeter sources, the sub-bands are

at such low signal-to-noise that they remain poorly constraining on the spectral index and flux density normalization. This effect is particularly striking for IGR J17544-2619, where the 40-GHz upper limit is strongly constraining on the power law shape when using the full ALMA bands; however, in the sub-bands, with ~ 2 times higher RMS uncertainties, these non-detections become consistent with a much broader range of spectral indices. Discussing IGR J17544-2619, we should also note that its full-ALMA-band SED does not appear to follow a single power law well; in fact, we may be observing the transition frequency, where the photosphere becomes smaller than the stellar radius, and the resulting flattening of the spectrum between the 40 and 100 GHz bands.

Comparing the fits with and without VLA data, only minor differences are found: slight changes, just beyond the 1σ confidence levels, are seen for the three brightest sources (4U 1700-37, Vela X-1, SAX J1818.6-1703). These result, as is visible in Figure 3, in slightly shifted but similar confidence regions for the model. In all three cases, these changes are driven by the lower radio flux densities or limits observed than extrapolated from the millimeter-only fit. The time difference between the observations may be responsible for these discrepancies, in particular for 4U 1700-37, where the deviation at 6 GHz is most significant – we will further discuss this scenario in Section 4.4.

4 DISCUSSION

In this work, we present a systematic study of the millimeter emission of twelve neutron star HMXBs. Combining existing and new ALMA and NOEMA observations, nine out of twelve targets are detected at one or more millimeter frequencies. These observations may shed light on the properties of the donor star’s wind in neutron star HMXBs, but may also be affected by non-thermal processes contributing at low frequencies. In this Discussion, we will investigate the origin of the detected low-frequency emission, before turning to inferences on the stellar wind properties. We will subsequently discuss additional constraints on the winds for systems that power a bow shock in the ISM, and will briefly discuss evidence for low-frequency variability in our sample.

4.1 The origin of radio – millimeter emission in SgXBs and SFXTs: stellar winds and/or jets?

To understand the origin of low-frequency emission in neutron star HMXBs, the evident comparison sources are low-mass X-ray binaries, Be/X-ray binaries, and OB supergiants without a compact object companion. Given those options, two primary sources of low-frequency radiation arise: relativistic jets launched from the accretion flow, or thermal emission from the outer stellar wind. The superposition of both processes may be observed, and it should be noted that the two are not fully independent: jet-wind interactions may shape and brighten the jet (e.g., [Zdziarski 2012](#); [López-Miralles et al. 2022](#)). OB supergiants residing in binaries with another massive star may also power intra-binary wind-wind collisions ([Dougherty et al. 2003](#); [Blout et al. 2022](#)); given the lack of such a companion in HMXBs, and the lack of evidence for strong disk winds, such wind-wind collisions are not likely relevant here (although see [Chatzis et al. 2022](#), for the expected radio emission from disk wind – stellar wind collisions). The optically thin spectra characteristic for such colliding wind binaries are also inconsistent with HMXB scenarios.

For the ionized, outer winds of massive stars, analytical models predict inverted radio to millimeter spectra ($\alpha > 0$), with a canonical

spectral index prediction of $\alpha = 0.6$ ([Wright & Barlow 1975](#); [Panagia & Felli 1975](#)). Observations of OB supergiants, as well as these analytical models, suggest specific radio luminosities in the range of $10^{17} - 10^{19}$ erg/s/Hz, with the upper end similar to that in extreme cases such as Wolf-Rayet stars ([Güdel 2002](#)). In the radio band, OB supergiant winds are therefore expected at $\sim 10^{26} - 10^{28}$ erg/s.

For relativistic jets, most spectral constraints exist for black hole X-ray binaries and neutron stars with low-mass donors. Steady jets in both types of systems are typically seen with flat or slightly inverted spectra ($\alpha \gtrsim 0$; [Fender & Kuulkers 2001](#)), but most typically not as inverted as the stellar wind regime. Such spectra are also seen, when multi-band observations are available, for the jets launched in Be/X-ray binaries (with the exception of an optically thin radio spectrum in the super-Eddington state of Swift J0243.6+6124; [van den Eijnden et al. 2018](#)). The jet’s luminosity, for strongly-magnetized neutron stars (like those in HMXBs; $B \gtrsim 10^{12}$ G; [Staubert et al. 2019](#)), is best measured in Be/X-ray binaries as well, given the weakness of the spherical stellar wind that complicates our interpretation here for SgXBs and SFXTs: interpolating the Be/X-ray binary jets to lower accretion rates, we expect a radio luminosity of the order $\sim 10^{26}$ erg/s at an accretion rate of $\sim 1\%$ Eddington, typical for a SgXB ([van den Eijnden et al. 2024](#)).

Several complications in these jet expectations remain, however: firstly, the interaction with the wind may brighten the jet, as discussed in [van den Eijnden et al. \(2024\)](#) for a so-called persistent Be/X-ray binary. Secondly, the Be/X-ray binary Swift J0243.6+6124 deviated from the extrapolation used above for Be/X-ray binary jet luminosities during brief X-ray re-brightenings. Therefore, the prediction above may be underestimated by two orders of magnitude, although the origin of this deviation is not well understood. On the other hand, the jets in Be/X-ray binaries are launched from an accretion disk, which is not likely to be present in most SgXBs and SFXTs (although see [El Mellah et al. 2018](#)); depending on the jet launch model, that may complicate the formation of the jet in the first place ([Massi & Kaufman Bernadó 2008](#); [Parfrey et al. 2016](#); [Das et al. 2022](#); [Das & Porth 2024](#)).

Given these two possible contributing processes (winds and jets) and the complications in predicting the jet scenario exactly, previous radio studies remained ambiguous on the emission’s origin. [Pestalozzi et al. \(2009\)](#), for instance, report radio monitoring of the neutron star + hypergiant system GX 301-2 / BP Cru, reporting variability in radio brightness and spectrum. Whether this is driven only by the stellar wind or includes an additional non-thermal component at certain orbital phases remains unconfirmed in their data, also due to the lower sensitivity in the pre-CABB ATCA data ([Wilson et al. 2011](#)). In [van den Eijnden et al. \(2021\)](#), the radio counterpart of five SgXBs is reported. However, the uncertainties on the spectral index, measured over the small range from 5.5 to 9 GHz, are too large to unambiguously associate this emission with either a wind, a jet, or their interaction.

The millimeter observations presented in this work help answer this question in more detail, particularly using the combined VLA and ALMA constraints for six targets. There, the frequency range from 6 to 300 GHz reveals strongly inverted low-frequency spectra, with the spectral index typically observed to lie in the range $\alpha \approx 0.6 - 0.8^2$. The spectral indices measured from NOEMA sub-bands do

² Interestingly, a similar spectral slope with $\alpha = 0.71 \pm 0.02$ was found in recent *JWST* MIRI observations of the black hole X-ray binary A0620-00 in its quiescent state, interpreted as thermal free-free emission from a strong and warm ($T_e \approx 10^4$ K) wind outflow from the accretion disc ([Zuo et al. 2025](#)).

not provide similar constraints, given their significant uncertainties and small fractional frequency differences. The specific luminosities measured in the millimeter bands range in the order of a few times 10^{17} to a few times 10^{18} erg/s/Hz at the lowest millimeter frequencies (40 or 100 GHz), which is comparable to the typical levels of early-type single and binary stars. The 300 GHz millimeter luminosity in 4U 1700-37, for instance, is comparable to the brightest 300 GHz luminosity seen from the jet in the neutron star low-mass X-ray binary Aql X-1 (Díaz Trigo et al. 2018); a jet interpretation in this SgXB would be at odds with the much fainter radio jets seen in Be/X-ray binaries than in neutron star low-mass X-ray binaries.

Given the new evidence from our radio + millimeter spectra, we conclude that these low-frequency SEDs are dominated by the thermal free-free emission from the stellar wind. For six sources, we do not have a spectrum but merely a single band NOEMA measurement (as the sub-bands are separated by a small fractional difference, we opt not to put much weight on the measured in-band spectral index). As the typical specific luminosities of those targets, when detected, are similar to the VLA+ALMA targets, we deem it most likely that their emission is similarly dominated by the stellar wind; no systematic difference in target selection was applied between the two sub-samples, beyond declination constraints per telescope.

In none of the six VLA + ALMA target can we see evidence for a radio jet dominating at lower frequencies, only to be taken over by a more inverted stellar wind spectrum in the millimeter band. To see to what degree that may be expected in future observations, we can perform an order of magnitude comparison of the expected luminosity of the stellar wind and jet in a neutron star HMXB. For this, we assume a stellar wind mass loss rate and velocity, from which we calculate the analytical thermal wind spectrum. Further assuming a $1.4 M_{\odot}$ neutron star, a donor star mass, and an orbital period, we can calculate the orbital velocity v_{orb} assuming a circular orbit and the ratio q of neutron star to total mass. Following Tejeda & Toalá (2025), we can then estimate the wind capture fraction as $\eta_{\text{cap}} = (q / (1 + (v_{\infty}/v_{\text{orb}})))^2$, which gives an X-ray luminosity of $L_X = 0.1 \eta_{\text{cap}} \dot{M}_{\text{w}} c^2$. Finally, we estimate the expected jet luminosity from the best-fit $L_X - L_R$ relation for Be/X-ray binaries reported in van den Eijnden et al. (2022). We emphasize that each of these steps in the calculation of the jet luminosity comes with statistical and systematic uncertainties, and therefore this comparison should be interpreted only at the order of magnitude level.

In Figure 4, we show the ratio of jet and wind luminosity as a function of wind mass loss rate, varying a number of the input parameters: the observing frequency, wind terminal velocity, jet spectral index, orbital period, and donor star mass. The black line shows the baseline case ($v_{\infty} = 1000$ km/s, $\nu = 10$ GHz, $M_{\text{donor}} = 20 M_{\odot}$, $P_{\text{orb}} = 10$ days, $\alpha_{\text{jet}} = 0$), while the legend shows the varied parameters for each of the other curves. From this order-of-magnitude comparison, we find that beyond 1 GHz frequencies, the jet is unlikely to dominate in the spectrum of SgXBs; even at low frequencies, that only occurs in specific circumstances. While these exact estimates will be affected by a range of complications – e.g., the wind acceleration profile, orbital eccentricity, uncertainties in the accretion rate – jet power relation – two conclusions can be drawn: if a combined spectrum, dominated by a jet at low frequencies, is observed in a SgXB in future campaigns, the jet’s luminosity is likely enhanced from interactions with the wind material. Secondly, the Be/X-ray binary jets dominate due to a combination of weak stellar wind and disk-accretion instead of wind-accretion, de-coupling the mass accretion rate from the stellar wind parameters.

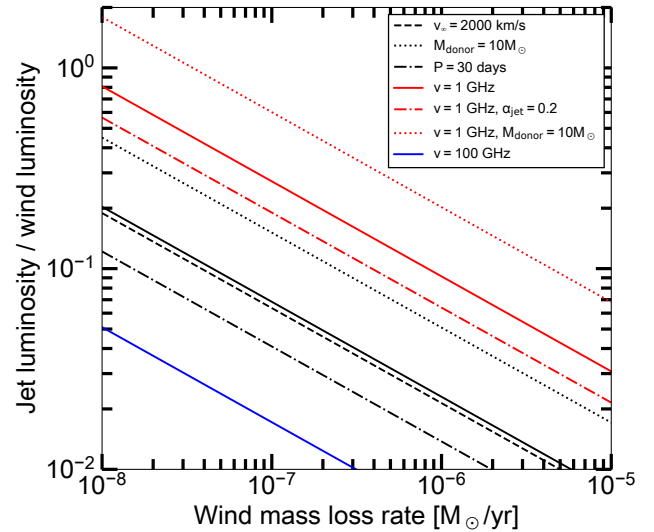


Figure 4. An order of magnitude comparison of the jet and wind luminosity assuming wind capture in a circular orbit and the measured Be/X-ray binary coupling between accretion rate and jet power. The legend indicates deviations from the standard input, shown as the black line ($v_{\infty} = 1000$ km/s, $\nu = 10$ GHz, $M_{\text{donor}} = 20 M_{\odot}$, $P_{\text{orb}} = 10$ days, $\alpha_{\text{jet}} = 0$). Despite the assumptions underlying this calculation, the jet is unlikely to be visible above 1 GHz unless interactions with the wind brighten it significantly.

4.2 Stellar wind properties in SgXBs and SFXTs

4.2.1 How do the millimeter properties of stellar winds compare between SFXTs and SgXBs?

The difference in X-ray behavior between SgXBs and SFXTs may be related to the properties of the donor star and its wind, the orbital parameters, the neutron star, and combinations thereof. As discussed in the reviews by Sidoli (2017) and Kretschmar et al. (2019), none of these three options individually offer an obvious explanation: the sample of known SFXTs and SgXBs shows significant overlap in their observables, such as donor star types, orbital periods, and neutron star spin periods. Differences in clumping structure in the winds are unlikely to account for the flaring behaviour in SFXTs, given the unrealistically large clump masses needed to power a typical X-ray flare. Through a detailed and consistent comparisons between two systems, the SFXT IGR J17544-2619 and SgXB Vela X-1, Giménez-García et al. (2016) suggested that the stellar wind in the SFXT may be significantly faster – leading to a lower capture rate and average X-ray luminosity. Similar arguments for the overall sample were made by, e.g., Negueruela (2019), arguing that the stellar types in SFXTs may be earlier and that therefore their winds may be faster. Alternatively, Hubrig et al. (2019) discussed the role of the stellar wind’s magnetic field in regulating the wind accretion process.

Whether any such systematic wind differences indeed exist and drive the behavioral dichotomy between SFXTs and SgXBs, remains, at the moment, unconfirmed. As we conclude that the millimeter emission of both types of systems is dominated by thermal wind emission, our data particularly allows us to investigate the case of different donor star properties. With this in mind, we show the re-scaled 100-GHz luminosity versus the orbital period of our targets in the left panel of Figure 5 (using the observed spectral index, or otherwise assuming $\alpha = 0.6$). Comparing the millimeter luminosity allows us to understand the role of source distance and removes

the differences due to the different NOEMA and ALMA observing frequencies. The four SFXTs in our sample (the circles) show a strikingly small range (~ 3.3) in millimeter luminosity, between 6×10^{28} erg/s and 2×10^{29} erg/s. The set of all six persistently accreting systems, on the other hand, trace a wider luminosity range (a factor ≥ 50), between $< 4.6 \times 10^{28}$ erg/s and 2.4×10^{30} erg/s. The intermediate system IGR J19140+0951 sits among the brightest millimeter sources.

A more detailed look at these millimeter luminosities – taking into account the properties of the individual SgXBs – reveals a potential difference between the SFXTs and the *classical* SgXBs. Firstly, 4U 2206+54 and 4U 1907+09 overlap with the millimeter luminosity range of the SFXTs. As noted earlier, while 4U 2206+54 is grouped with the SgXBs given its persistently accreting nature, its donor is not a supergiant but a O9.5V star (Blay et al. 2006). 4U 1907+09 does host a supergiant donor, but displays dipping behaviour in X-rays that has been suggested to be similar to the X-ray flaring in SFXTs, which would make it a link between the two sub-classes (Doroshenko et al. 2012). On the other hand, the three millimeter-detected SgXBs with higher 100-GHz luminosities are bona fide SgXBs, in particular the prototypical SgXBs Vela X-1 and 4U 1700-37. We may therefore interpret our results as showing a systematically higher millimeter luminosity in prototypical SgXBs than in SFXTs.

To further investigate and substantiate this claim, we also perform a comparison between millimeter luminosities and the equivalent width (EW) of the 6.4 keV Fe $K\alpha$ line. This emission line, in HMXBs, originates from the fluorescence in the stellar wind material of X-rays emitted by the accretion flow close to the neutron star. A higher density of wind material therefore leads to a larger EW. The EW is known to correlate with the absorption column density in X-rays (Pradhan et al. 2018), which is expected for such higher densities of fluorescing material (see also Torrejón et al. 2010b; Giménez-García et al. 2015). Strikingly, Pradhan et al. (2018) report that SgXBs trace a significantly larger range in EW and absorption column than SFXTs, where the SFXTs only overlap with the low end of the EW and absorption column measurements in SgXBs – behaviour somewhat reminiscent of the millimeter luminosities discussed above.

For each target in our sample, we therefore take all measurements of the Fe $K\alpha$ EW from Pradhan et al. (2018), regardless of X-ray properties during the observation; instead, we calculate a weighted average of the EW for our comparison. We obtain EW measurements for all targets except 4U 2206+54 and 4U 1907+09 – precisely the two sources overlapping in millimeter luminosity with the SFXTs and with complication in their SgXB classification. In addition, we take the SgXBs included in the radio compilation of van den Eijnden et al. (2021) and perform a similar cross-match. This literature addition adds the SgXBs OAO 1657-415, 4U 1538-522, EXO 1722-363, IGR J16207-5129, IGR J16318-4848, and IGR J16320-4751 to the sample. Finally, we add GX 301-2 (BP Cru), based on Pestalozzi et al. (2009). These literature-based SgXBs were all observed with ATCA at 5.5 and 9 GHz. The first four systems in the list are not detected in either band; we therefore take their 9-GHz 3σ upper limit and extrapolate to 100-GHz assuming a standard spectral index $\alpha = 0.6$. For IGR J16320-4751 and GX 301-2, we assume the same spectral shape to extrapolate their 5.5 GHz and highest-significance 9-GHz detections, respectively. Finally, for IGR J16318-4848, we extrapolate its combined 5.5 and 9 GHz detections to higher frequency through a Monte-Carlo simulation. We stress that these extrapolations, and comparison with our millimeter-observed sample, implicitly assume their low-frequency SED is stellar-wind dominated.

The resulting comparison of millimeter luminosity and EW is shown in the right panel of Figure 5, where millimeter limits are

shown semi-transparently and literature-based extrapolations only with errorbars. We observe a confirmation that the SFXTs are millimeter-underluminous compared to the SgXBs with EW measurements. As the SgXBs included in this comparison generally show higher EWs than the SFXTs, we find that the SgXBs typically inhabit a different region of the EW- L_{mm} parameter space than SFXTs. We do note that the (extrapolated) millimeter upper limits for non-detected SgXBs are not constraining, currently, compared to the SFXT luminosity range; deeper observations can therefore further confirm this suggested dichotomy.

How can we physically interpret this apparent difference between the compared SgXB and SFXTs? Discussing the EW (and its correlation with absorption column), Pradhan et al. (2018) discuss two interplaying scenarios: firstly, an overall faster wind in SFXTs would lead to a lower density at the neutron star’s position and lower rates of gas capture. Secondly, bright accretion-driven X-ray emission slows down the wind in the vicinity of the neutron star by ionizing the wind material and inhibiting the wind acceleration mechanism, regardless of the overall wind velocity. Such ionizing emission is however, typically, significantly weaker in SFXTs compared to SgXBs. The lower wind density leads to a lower EW if the Fe $K\alpha$ emission predominantly originates from the regions close to the neutron star.

The millimeter luminosity of our targets provides a large-scale view of the stellar wind in comparison to the small-scale constraints from the EW. Interestingly, these large-scale and small-scale results present a similar picture: the thermal millimeter emission is a probe of the wind density on scales beyond the binary orbit, which decreases for a higher global wind velocity. Barring systematic differences in mass loss rate between the SFXTs and SgXBs, a systematically lower wind velocity may account for the brighter millimeter emission from large scales in SgXBs and a higher Fe $K\alpha$ EW from scales close to the neutron star.

4.2.2 How do the millimeter properties of stellar winds compare with literature estimates?

Beyond comparing the stellar wind properties as probed in the low-frequency SED between source classes, we can also compare with literature estimates. For that purpose, the observed low-frequency spectrum should be converted to physical properties that can be compared to independent measurements. Specifically, we will use the millimeter luminosity as a proxy for the ratio of mass-loss rate and wind terminal velocity, following the analytical derivations by Wright & Barlow (1975); Panagia & Felli (1975) introduced priorly. Before doing so, we reiterate that this classic, analytical understanding of the low-frequency emission does not fully explain the observed SEDs of our targets: most strikingly, we observe spectral indices that are inverted, but differ from the expected $\alpha = 0.6$, possibly reflecting that the wind may not have reached its terminal velocity in the dominant millimeter emission regions.

The normalization of the thermal wind SED with spectral index $\alpha = 0.6$, in the analytical models, depends on the temperature of the wind, its composition, the distance to the target, and, crucially, the wind density. Under the assumption of a smooth and spherically symmetric wind, mass conservation, and a constant velocity (which are re-evaluated in our companion work) the radial density profile follows from the mass loss rate and velocity. As a result, analytically, the thermal wind flux at radio or millimeter frequency ν is expected to scale as (see also Güdel 2002, for the exact numerical constants)

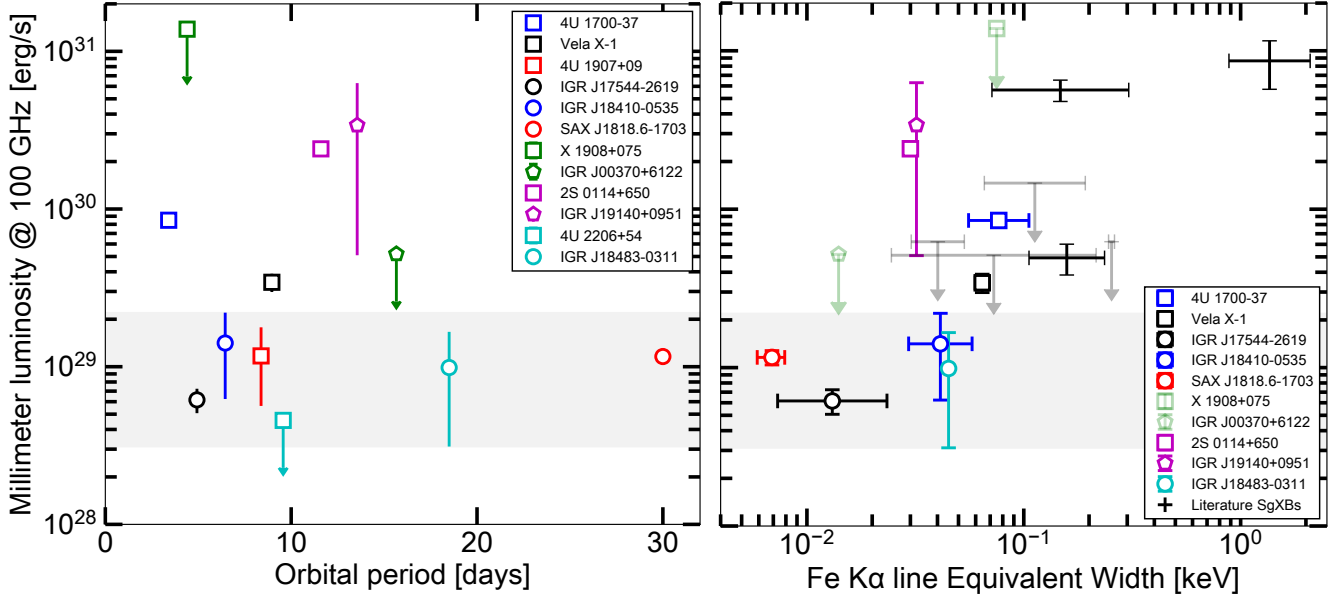


Figure 5. *Left:* The 100-GHz millimeter luminosities versus orbital period. SgXBs are shown as squares; SFXTs as circles; intermediate sources as pentagons. The uncertainties on the millimeter luminosity include both flux density and distance uncertainties. *Right:* the millimeter luminosity plotted versus the Equivalent Width of the Fe K α line at 6.4 keV. Archival points are shown based on [van den Eijnden et al. \(2021\)](#), under the assumption that these extrapolated radio luminosities are dominated by stellar wind emission. In both panel, the grey band indicated the range covered by SFXTs.

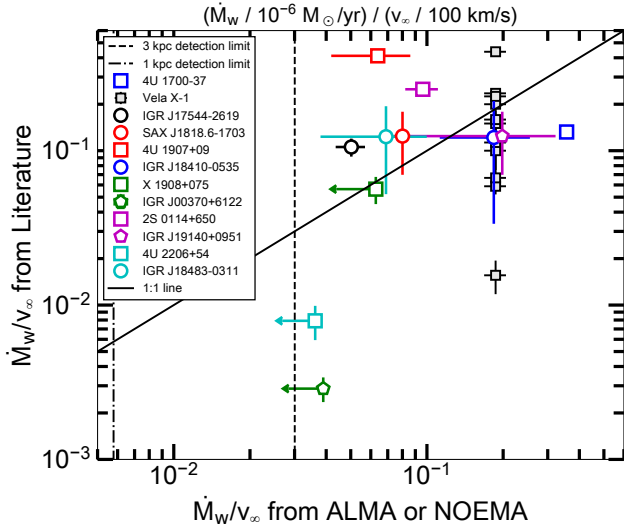


Figure 6. A comparison of the constraints on $\dot{M}_{\text{w}}/v_{\infty}$ from millimeter observations and from literature measurements. Vela X-1 shown as a vertical band reflecting the range of literature measurements; for all other sources, a single literature value is plotted. Squares indicate SgXBs, circles SFXTs and intermediates. The four SFXTs/intermediates sharing the same approximate literature value were plotted using estimates given their stellar type, explaining their similar vertical level.

$$S_{\nu} \propto \left(\frac{\dot{M}_{\text{wind}}}{v_{\infty}} \right)^{4/3} \nu^{6/10}. \quad (1)$$

Therefore, assuming similar compositions and wind temperatures

(although the flux density depends only weakly on temperature), we can use our millimeter measurements as a proxy for $\dot{M}_{\text{wind}}/v_{\infty}$. Through alternative measurements, this ratio can similarly be constrained, particularly allowing for a comparison of our millimeter results with probes of the inner stellar wind.

For this purpose, we compiled literature measurements of the stellar wind mass loss rates and velocities for all our targets, obtained from optical / UV spectroscopy and therefore probing the inner wind regions. For eight out of twelve sources, at least one such measurement was available, as summarized in Table 5. For the other four targets (IGR J18410-0535, SAX J1818.6-1703, IGR J19140+0951, and IGR J18483-0311), we instead match their stellar type to the closest comparison(s) in [Crowther et al. \(2006\)](#) and [Markova & Puls \(2008\)](#). We then use the reported wind properties of those closest matches to calculate a typically expected $\dot{M}_{\text{wind}}/v_{\infty}$, with an uncertainty representing the spread in values amongst these matched sources. We note that, for all twelve targets, the statistical uncertainties on literature mass loss rates and velocities may be smaller than those from the millimeter constraints. However, systematic uncertainties in the underlying method likely introduce more significant errors $\dot{M}_{\text{wind}}/v_{\infty}$ than we report here.

In Figure 6, we show the comparison between $\dot{M}_{\text{wind}}/v_{\infty}$ based on the millimeter emission at 100 GHz (extrapolated from 150 GHz for ALMA targets using the measured ALMA-based α) and based on literature values using optical or UV spectroscopy – in other words, a comparison between outer and inner wind diagnostics. All sources are shown with the same markers as in other plots, except Vela X-1: the smaller grey-filled black squares indicates the range of different measurements of $\dot{M}_{\text{wind}}/v_{\infty}$ from the large number of archival studies. Overall, we do not observe that the sample follows the potentially expected one-to-one relation. Instead, we can identify several types of behavior in this diagram: firstly, the four targets matched to earlier studies of other B-type supergiants align in their literature value, and match the one-to-one line within uncertainties.

Secondly, four systems lie significantly away from the 1 : 1 relation: 4U 1700-37 below the relation, versus 4U 1907+09, 2S 0114+650, and IGR J17544-2619, above. Finally, the three systems that are not detected in millimeter, the non-detection is consistent with their inner wind constraints in all cases.

The three systems lying above the relation may be accounted for by radially-dependent clumping (Sundqvist et al. 2018): clumping can lead to overestimates of the mass-loss rate at a given velocity, increasing $\dot{M}_{\text{wind}}/v_{\infty}$. If the degree of clumping decreases radially towards the outer wind, systems may then be pushed above the 1:1 relation in this figure. Indeed, for two of these three sources, 4U 1907+09 and 2S 0114+650, clumping was not taken into account when estimating the stellar wind parameters (Cox et al. 2005; Reig et al. 1996). In the third, IGR J17544-2619, Giménez-García et al. (2016) did include clumping in their modeling of the IR, optical, and UV spectra. However, the degree of clumping could not be determined self-consistently and the authors note that more work is needed; therefore, it may be possible that the inferred wind parameters are affected by an underestimate of the degree of clumping. This work analysed Vela X-1 through the same approach, managing to determine the clumping more confidently. This is reflected by the resulting ratio of $0.09^{+0.06}_{-0.04}$ in our units. This measurement for Vela X-1 is close to the millimeter value of 0.19 ± 0.02 , albeit slightly lower: opposite to sources where clumping affects the measurement.

Vela X-1 is, generally, a special case in this comparison due to its range of archival estimates. The biggest outliers, both above and below the millimeter constraint, were obtained in early estimates (Conti 1978; Dupree et al. 1980; McCray et al. 1984; Sadakane et al. 1985; Sako et al. 1999) that also typically constrain either mass loss rate or velocity after assuming the other from earlier works. More recent works align more closely with the millimeter measurements, reporting ratios in the range 0.1 – 0.2 based on X-ray line measurements Watanabe et al. (2006) or wind modeling with the explicit inclusion of X-ray irradiation (Krtićka et al. 2012; Sander et al. 2018). While these measurements may be below the millimeter constraint, they do not deviate as significantly as 4U 1700-37. In those cases, variability in the wind may play a role: indeed, as we will discuss in Section 4.4, both Vela X-1 and 4U 1700-37 show evidence for slow variability in their low-frequency measurements. That would imply, however, that any effects of variability in other sources are smaller than the effects of clumping and measurement uncertainties.

4.3 Combining millimeter with bow shock constraints

The SgXBs Vela X-1 and 4U 1907+09 are the two only known neutron star HMXBs that create an observed bow shock in the ISM³. A bow shock is formed when an object moves supersonically in the ISM, where the speed of sound for a standard density and temperature ($\sim 1 \text{ cm}^{-3}$ and $\sim 10^4 \text{ K}$) is of the order 10 km/s. For runaway massive stars, ejected from their birth stellar population via dynamical or supernova-driven ejection mechanisms (Poveda et al. 1967; Blaauw 1961), the bow shock is formed at a distance from the star: at this stand-off distance, the combined thermal and ram pressure of the ISM, moving at the stellar velocity in the frame of the star, equals the ram pressure of the wind moving at its terminal velocity. As a result, the stand-off distance R_0 can be related to the stellar wind

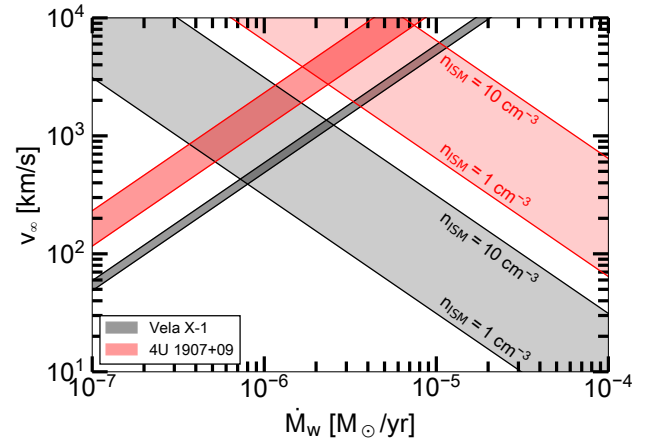


Figure 7. A comparison of the constraints on stellar wind mass loss rate and terminal velocity from millimeter observations (increasing curves) and bow shocks (decreasing curves). The latter is shown for a range of ISM densities, ignoring the second order effect of thermal ISM pressure.

parameters, peculiar stellar velocity v_* , and ISM properties (density n_{ISM} , temperature T_{ISM}), to write:

$$\begin{aligned} \dot{M}_w v_{\infty} &= 4\pi n_{\text{ISM}} R_0^2 \left(m_p v_*^2 + k T_{\text{ISM}} \right) \\ &\approx 4\pi m_p n_{\text{ISM}} R_0^2 v_*^2, \end{aligned} \quad (2)$$

where m_p is the proton mass and the approximation is accurate for $T_{\text{ISM}} < 10^4 \text{ K}$ to within 2.7% and 0.3% for Vela X-1 ($v_* \approx 55 \text{ km/s}$; Gvaramadze et al. 2018) and 4U 1907+09 ($v_* \approx 160 \text{ km/s}$; Gvaramadze et al. 2011), respectively. The stand-off distance is resolvable for both objects (0.57 pc and 0.89 pc, respectively), and hence the product of mass-loss rate and terminal velocity can be constrained.

In Figure 7, we show the regions in the mass-loss rate and terminal velocity space that are permitted for Vela X-1 and 4U 1907+09, based on their millimeter emission and their bow shocks. For the latter, we plot the constraints assuming an ISM density between 1 and 10 cm^{-3} . The band shown for the former represents the flux density uncertainty in the millimeter band and distance uncertainty. We find that the constraints for Vela X-1 intersect at $\dot{M}_w \approx 8 \times 10^{-7} (n_{\text{ISM}} / 1 \text{ cm}^{-3})^{1/2} M_{\odot}/\text{yr}$ and $v_{\infty} = 4 \times 10^2 (n_{\text{ISM}} / 1 \text{ cm}^{-3})^{1/2} \text{ km/s}$; for 4U 1907+09, we find $\dot{M}_w \approx 2 \times 10^{-6} (n_{\text{ISM}} / 1 \text{ cm}^{-3})^{1/2} M_{\odot}/\text{yr}$ and $v_{\infty} = 3 \times 10^3 (n_{\text{ISM}} / 1 \text{ cm}^{-3})^{1/2} \text{ km/s}$. These values for Vela X-1 are consistent with recent literature measurements (e.g., Table 5) for ISM densities of the order a few per cm^3 – a density consistent with constraints from modelling its bow shock in the radio band (van den Eijnden et al. 2022). For 4U 1907+09, a density below 1 cm^{-3} is needed to match earlier estimates in the literature.

4.4 Variability in low-frequency stellar wind emission

A search for intra-observational variability in the ALMA observations did not reveal millimeter flaring nor flux density evolution on short (\sim minutes) time scales. For a subset of targets and observing bands, that may not be surprising, given the insufficient signal-to-noise: we can estimate a minimum signal-to-noise in the time-integrated observation of length T required for a $\geq 3\sigma$ detection in each time bin of length Δt and a constant source, as $3\sqrt{T/\Delta t}$. For, e.g., $\Delta t = 1 \text{ minute}$, only 4U 1700-37, Vela X-1, and Bands 4 and 7 of SAX J1818.6-0535 reach this requirement. For those

³ We note that the SFXE IGR J17544-2619 is runaway system as well (Macarone et al. 2014). Because its proper motion is dominated by its radial motion, no bow shock is seen in IR, optical, or radio.

Table 5. The literature constraints on mass-loss rate and terminal velocity, with uncertainties taken from the literature when mentioned in the original reference (final column). For the four targets without literature estimates, we show the mean and standard deviation in measurements of \dot{M}_w/v_∞ in stars of similar types (final column) from [Crowther et al. \(2006\)](#) and [Markova & Puls \(2008\)](#). Here, \dot{M}_w/v_∞ is calculated after re-scaling the mass-loss rate to $10^{-6} M_\odot/\text{yr}$ and the terminal velocity of 100 km/s. *For Vela X-1, we show the range in mass-loss rates and terminal velocities as reported in the literature and compiled by [Kretschmar et al. \(2021\)](#). Original values were reported in [Conti \(1978\)](#); [Dupree et al. \(1980\)](#); [McCray et al. \(1984\)](#); [Sadakane et al. \(1985\)](#); [Sato et al. \(1986\)](#); [Sako et al. \(1999\)](#); [Watanabe et al. \(2006\)](#); [Krtićka et al. \(2012\)](#); [Falanga et al. \(2015\)](#); [Manousakis & Walter \(2015\)](#); [Giménez-García et al. \(2016\)](#); [Sander et al. \(2018\)](#).

Name	Mass-loss rate [M_\odot/yr]	Terminal velocity [km/s]	Method	Reference
4U 1700-37	$(2.5^{+2.5}_{-1.3}) \times 10^{-6}$	1900 ± 100	UV/optical	Hainich et al. (2020)
Vela X-1	$(0.265 - 2.4) \times 10^{-6}$	532 – 1700	UV/optical/X-rays	Kretschmar et al. (2021)*
4U 1907+09	7×10^{-6}	1700 ± 30	UV/optical	Cox et al. (2005)
IGR J17544-2619	$(1.6^{+0.9}_{-0.6}) \times 10^{-6}$	1500 ± 200	UV/optical/IR	Giménez-García et al. (2016)
X1908+075	2.8×10^{-7}	500 ± 100	IR	Martínez-Núñez et al. (2015)
IGR J00370+6122	$(3.2^{+1.8}_{-1.2}) \times 10^{-8}$	(1100 ± 200)	UV/optical	Hainich et al. (2020)
2S 0114+650	3×10^{-6}	1200	Optical/IR	Reig et al. (1996)
4U 2206+54	$(3.2^{+3.1}_{-1.7}) \times 10^{-8}$	400 ± 100	UV/optical	Hainich et al. (2020)
	Mean \dot{M}_w/v_∞	St. Dev. \dot{M}_w/v_∞	Stellar type	Comparison types
IGR J18410-0535	0.122	0.088	B1Ib/B0.2Ibp/B1I	B1Ia/B1Iab
SAX J1818.6-1703	0.124	0.054	B0.5Iab	B0.5Ia
IGR J19140+0951	0.124	0.054	B0.5Ia	B0.5Ia
IGR J18483-0311	0.123	0.071	B0.5-B1	B0.5Ia/B1Ia/B1Iab

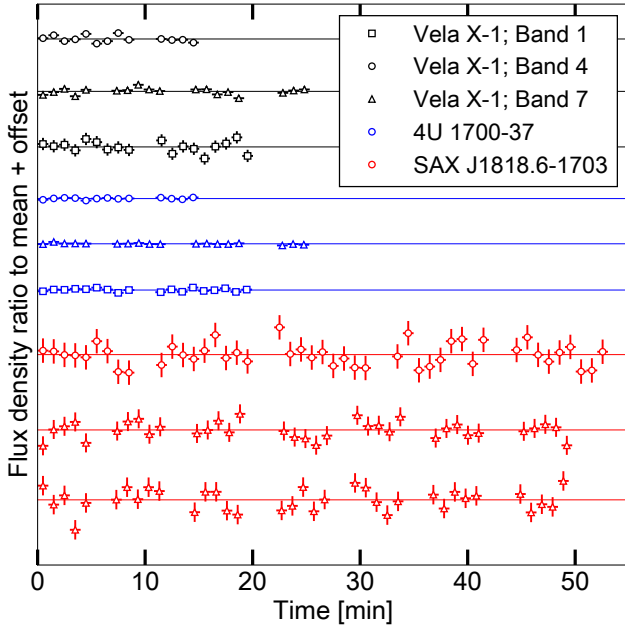


Figure 8. The ALMA 1-minute light curves for the targets and observing bands where the signal-to-noise is sufficient to detect the target in each time bin at $\geq 3\sigma$. Each light curve has been re-scaled by its mean and given an arbitrary vertical offset for clarity. Errors are shown at the 1σ level. The SAX J1818.6-1703 Band 7 light curve consists of two parts, as the full observation exceeded a single observing block.

sources/observing bands, we can calculate the reduced χ^2 of a constant fit to the 1-minute light curve as a first assessment of variability. In all cases, $\chi^2_{\nu, \text{constant}} \leq 1$, implying the light curves are consistent with being constant. These light curves, re-scaled to their mean and shown with a vertical offset, are shown in Figure 8.

Alternatively, we can convert this non-detection of variability in an upper limit on fractional variability. The fractional variability F_{var} , as defined by [Vaughan et al. \(2003\)](#), cannot be calculated for cases where $\chi^2_{\nu, \text{constant}} \leq 1$, as this statement is equivalent to the variance S^2 being smaller than the mean square error σ_{err}^2 (see their Equation 9). To understand the minimum detectable fractional variability at 3σ , we can assess when $F_{\text{var}} > 3 \times \text{err}(F_{\text{var}})$. In the low-variability regime (e.g., the first case of Equation B1 in [Vaughan et al. \(2003\)](#)), this is equivalent to a minimum detectable fractional variability of

$$F_{\text{var, detectable}} \geq \left(\frac{9}{2N} \right)^{\frac{1}{4}} \frac{\sqrt{\sigma_{\text{err}}^2}}{\bar{S}_\nu}, \quad (3)$$

where N is the number of bins and \bar{S}_ν is the mean flux density in the light curve. Further assuming that the uncertainty in each time bin scales with \sqrt{N} , this limit is equivalent with

$$F_{\text{var, detectable}} \geq \left(\frac{9}{2N} \right)^{\frac{1}{4}} \text{SNR}^{-1}, \quad (4)$$

where SNR equals the signal-to-noise ratio of the full observation. This calculation implies the limits on the fractional variability at a 1 minute time scale are 0.5% / 0.4% / 0.3% for 4U 1700-37 (Band 1/4/7); 2% / 1.5% / 1% for Vela X-1 (Band 1/4/7); and 2.1% / 1.9% for SAX J1818.6-0535 (Band 4/7).

On time scales beyond individual observations, several approaches can be taken to assess the presence of variability. For instance, the comparison of the three ALMA bands, expected to lie on a single spectrum, did not reveal obvious variability between days of observations. On longer time scales, however, evidence for low-frequency variability can be found along different paths.

Firstly, IGR J18410-0535 was detected first with NOEMA in February 2023 at $63.4 \pm 9.6 \mu\text{Jy}$. The ALMA observations, all taking place in October 2024, revealed a spectrum at lower flux density; the SED fit returns a 100 GHz range of $\sim 20 - 30 \mu\text{Jy}$. Given the systematic uncertainty on the NOEMA and ALMA flux density scale

of the order $\lesssim 10\%$, such a factor ~ 2 variation appears intrinsic to the source. Secondly, in the radio band, 4U 1700-37 is observed at significantly lower flux densities ($\sim 250 \mu\text{Jy}$ at 6 GHz) than during the 2018 ATCA observations ($484 \pm 13 \mu\text{Jy}$ at 5.5 GHz) presented in van den Eijnden et al. (2021). Again, a factor ~ 2 variability is seen, with a potentially shallower ($\alpha = 0.46 \pm 0.16$) radio spectrum in 2018 than in millimeter in 2024 ($\alpha = 0.70 \pm 0.01$ from ALMA and VLA). Finally, the Vela X-1 VLA radio spectrum appears potentially shallower ($\alpha = 0.36 \pm 0.33$) than the millimeter spectrum ($\alpha = 0.78 \pm 0.02$), with ~ 12 days separating the radio and millimeter observations.

From the inverted spectra we earlier assumed that the same thermal wind emission underlies the low-frequency spectrum at all different epochs. For such a spectrum, changes in the emission can be driven by global changes in the wind mass loss rate or its velocity. To estimate the time scales of such variability, we can follow Güdel (2002) and write for the optically thick radius of the stellar wind

$$R_{\text{thick}} = 3.6 \times 10^2 R_{\odot} \left(\frac{\dot{M}_w}{10^{-6} M_{\odot}/\text{yr}} \right)^{2/3} \left(\frac{v_{\infty}}{1000 \text{ km/s}} \right)^{-2/3} \times \left(\frac{T_e}{10^4 \text{ K}} \right)^{-9/20} \left(\frac{\nu}{100 \text{ GHz}} \right)^{-7/10}. \quad (5)$$

Any significant change in the emission across such a scale, originating from a change in global parameters of the wind, will require at least a causal time scale of variability $\tau_{\text{thermal}} \propto R_{\text{thick}}/v_{\infty}$, which we can write as

$$\tau_{\text{thermal}} \approx 2.9 \text{ days} \left(\frac{\dot{M}_w}{10^{-6} M_{\odot}/\text{yr}} \right)^{2/3} \left(\frac{v_{\infty}}{1000 \text{ km/s}} \right)^{-5/3} \times \left(\frac{T_e}{10^4 \text{ K}} \right)^{-9/20} \left(\frac{\nu}{100 \text{ GHz}} \right)^{-7/10}. \quad (6)$$

Variability on days time scale, and beyond, in the millimeter band can therefore be consistent with changes in the large-scale thermal emission reflecting changes in global wind parameters.

The stellar winds of B-type supergiants are known to be variable from studies focusing on singles or non-degenerate binaries. Such studies often focus on the detection of variability periods in photometry or, alternatively, $H\alpha$ properties (Kaufer et al. 2006; Lefever et al. 2007; Lefèvre et al. 2009), which have been linked to opacity-driven oscillations in the star (Kraus et al. 2015). Radial pulsations have, in particular, been linked to variability in the mass loss rates of the star (Glatzel et al. 1999; Yadav & Glatzel 2016). In addition, as the stellar winds are radiatively driven, instabilities in the wind driving mechanism may further lead to variable outflow rates. Focusing on measurements of the wind parameters instead of variability, significant changes have indeed been observed: while Prinja & Howarth (1986) reported variations in mass-loss rates of $\sim 10\%$ on \geq days time scales, Lefever et al. (2007), Kraus et al. (2015), and Haucke et al. (2018) report changes by factors 1.05 to 2.7 between observations separated by a day to \sim a year. Alternatively, Kaper et al. (1996) and Massa et al. (2024) performed systematic UV studies of a sample of ten and twenty-five OB stars, respectively, with Massa et al. (2024) for instance reporting an average 1σ variation in mass-loss rate of 22% – although individual stars range between 8% and 45% .

The analyses above focus on the wind variability from diagnostics probing into the inner wind regions. However, if such changes propagate to the large-scale millimeter and radio emitting regions, their magnitude would be sufficient to explain factor ~ 2 changes in the low-frequency SED normalization in SgXBs. This approach

ignores the complex environment created by the presence of the compact object; the presence of large-scale wakes, and potential induced variability in the wind structure. The small number of measurements of the low-frequency SgXB emission in this work, prevents a more detailed analysis taking into account such effects; in a future work, we aim to analyse these processes in the radio/millimeter variability of SgXBs in more detail.

5 CONCLUSIONS

We performed a first systematic millimeter study of a sample of neutron star HMXBs, focusing on twelve SgXBs and SFXTs using ALMA, NOEMA, and the VLA. In this work, we presented the results from these observations and focused in particular on the origin of their low-frequency emission and on the comparison between the two subclasses of targets. From our work, we draw the following conclusions:

(i) Using a combination of ALMA, NOEMA, and VLA observations, nine out of the twelve SgXBs and SFXTs were detected in at least one observing band. Two of the non-detected targets are SgXBs, while the third is an intermediate source. These non-detections are not explained merely by distance (Table 2)

(ii) Based on the spectral shapes and specific luminosities of the targets, we conclude that the radio and millimeter emission of neutron star SgXB and SFXTs is dominated by thermal free-free stellar wind emission.

(iii) In neutron star SgXBs and SFXTs, jet emission is unlikely to be detected, unless an SED is measured with a sufficient number of bands down to sub-GHz frequencies so that a flattening of the spectrum towards low frequencies can be measured. However, even then a favorable binary configuration and/or brightening of the jet compared to Be/X-ray binaries due interactions with wind material, is required to observe these jet signatures.

(iv) The millimeter band shows evidence for systematic differences between the stellar winds in SFXTs and SgXBs. In particular, the four SFXTs discussed in this work are intrinsically fainter at 100 GHz than prototypical SgXBs (e.g., Vela X-1, 4U 1700-37, 2S 0114+650) and SgXB detected in the radio band priorly (GX 301-2, IGR J16318-4848, and IGR J16320-4751). As these SgXBs also show typically stronger Fe $K\alpha$ lines, we find an agreement between probes of the stellar wind density on global scales and local scales close to the neutron star. A globally denser (e.g., because slower) stellar wind in SgXBs could explain both effect qualitatively, which we will explore quantitatively in a companion work.

(v) The observed low-frequency spectra are slightly more inverted than the analytical stellar wind spectral shapes predicted by Wright & Barlow (1975) and Panagia & Felli (1975). Applying the analytical prescriptions nonetheless, we find constraints on mass-loss rate over wind velocity that are inconsistent with the literature for several sources. Wind clumping, wind variability, and progressive wind acceleration may underlie these differences.

(vi) For Vela X-1, the millimeter constraints on the wind parameters agree with geometrical bow shock constraints for reasonable ISM densities. For 4U 1907+09, low ISM densities ($n_H < 1 \text{ cm}^{-3}$) are required.

(vii) No fast millimeter variability (e.g., within observations) is seen down to low values of the fractional variability, as expected for thermal wind emission. On longer time scales (e.g., at least several days), where the wind may causally variable, we find evidence for variability that warrants dedicated follow-up observations for further confirmation.

6 ACKNOWLEDGMENTS

For the purpose of open access, the authors have applied a Creative Commons Attribution (CC-BY) license to any Author Accepted Manuscript version arising from this submission. The authors thank all telescope operators for their work during the observations underlying this research; Edwige Chapillon for their assistance in NOEMA data reduction and imaging; and Karan Kumar for discussions about runaway high-mass X-ray binaries in Gaia DR3. JvdE is supported by funding from the European Union's Horizon Europe research and innovation programme under the Marie Skłodowska-Curie grant agreement No 101148693 (MeerSHOCKS) and acknowledges a Warwick Astrophysics prize post-doctoral fellowship made possible thanks to a generous philanthropic donation. This paper makes use of the following ALMA data: ADS/JAO.ALMA#2024.1.00657.S. ALMA is a partnership of ESO (representing its member states), NSF (USA) and NINS (Japan), together with NRC (Canada), NSTC and ASIAA (Taiwan), and KASI (Republic of Korea), in cooperation with the Republic of Chile. The Joint ALMA Observatory is operated by ESO, AUI/NRAO and NAOJ. The National Radio Astronomy Observatory is a facility of the National Science Foundation operated under cooperative agreement by Associated Universities, Inc. This work is based on observations carried out under project number w23bo with the IRAM NOEMA Interferometer. IRAM is supported by INSU/CNRS (France), MPG (Germany) and IGN (Spain). The research leading to these results has received funding from the European Union's Horizon 2020 research and innovation program under grant agreement No 101004719 [Opticon RadioNet Pilot ORP]. This research has made use of NASA's Astrophysics Data System Bibliographic Services and the SIMBAD database, operated at CDS, Strasbourg, France. This work made use of *ASTROPY*⁴, a community-developed core Python package and an ecosystem of tools and resources for astronomy (Astropy Collaboration et al. 2013, 2018, 2022), *EMCEE* (Foreman-Mackey et al. 2013), and *NUMPY* (Harris et al. 2020).

DATA AVAILABILITY

A GitHub reproduction repository will be made public upon acceptance of this paper and will contain all files to repeat the data reduction and analysis presented in this paper. An archived and stable release of this reproduction repository at the time of paper acceptance will also be made available on Zenodo. Raw data associated with this work will be available in their respective observatory archives after a one-year proprietary period. Earlier access after acceptance of the paper may be granted by the PI upon reasonable request.

REFERENCES

Aharonian F., Yang R., de Oña Wilhelmi E., 2019, *Nature Astronomy*, **3**, 561
 Aharonian F., et al., 2024, *ApJL*, **970**, L21
 Andersson E. P., Agertz O., Renaud F., 2020, *MNRAS*, **494**, 3328
 Andrews H., Fenech D., Prinja R. K., Clark J. S., Hindson L., 2019, *A&A*, **632**, A38
 Astropy Collaboration et al., 2013, *A&A*, **558**, A33
 Astropy Collaboration et al., 2018, *AJ*, **156**, 123
 Astropy Collaboration et al., 2022, *ApJ*, **935**, 167
 Belczynski K., Bulik T., Fryer C. L., Ruiter A., Valsecchi F., Vink J. S., Hurley J. R., 2010, *ApJ*, **714**, 1217

Benaglia P., Koribalski B., 2007, in St. -Louis N., Moffat A. F. J., eds, *Astronomical Society of the Pacific Conference Series Vol. 367, Massive Stars in Interactive Binaries*. p. 179
 Benaglia P., Vink J. S., Martí J., Maíz Apellániz J., Koribalski B., Crowther P. A., 2007, *A&A*, **467**, 1265
 Bieging J. H., Abbott D. C., Churchwell E. B., 1989, *ApJ*, **340**, 518
 Blaauw A., 1961, *Bull. Astron. Inst. Netherlands*, **15**, 265
 Blay P., Negueruela I., Reig P., Coe M. J., Corbet R. H. D., Fabregat J., Tarasov A. E., 2006, *A&A*, **446**, 1095
 Blomme R., van de Steene G. C., Prinja R. K., Runacres M. C., Clark J. S., 2003, *A&A*, **408**, 715
 Bloot S., Callingham J. R., Marcote B., 2022, *MNRAS*, **509**, 475
 Bozzo E., Oskinova L., Feldmeier A., Falanga M., 2016, *A&A*, **589**, A102
 Bozzo E., Ducci L., Falanga M., 2021, *MNRAS*, **501**, 2403
 Bykov A. M., Petrov A. E., Ponomaryov G. A., Levenfish K. P., Falanga M., 2024, *Advances in Space Research*, **74**, 4276
 CASA Team et al., 2022, *PASP*, **134**, 114501
 Chatzis M., Petropoulou M., Vasilopoulos G., 2022, *MNRAS*, **509**, 2532
 Coleiro A., Chaty S., 2013, *ApJ*, **764**, 185
 Conti P. S., 1978, *A&A*, **63**, 225
 Cox N. L. J., Kaper L., Makiem M. R., 2005, *A&A*, **436**, 661
 Crowther P. A., Lennon D. J., Walborn N. R., 2006, *A&A*, **446**, 279
 Daley-Yates S., Stevens I. R., Crossland T. D., 2016, *MNRAS*, **463**, 2735
 Das P., Porth O., 2024, *ApJL*, **960**, L12
 Das P., Porth O., Watts A. L., 2022, *MNRAS*, **515**, 3144
 Díaz Trigo M., et al., 2018, *A&A*, **616**, A23
 Diez C. M., et al., 2022, *A&A*, **660**, A19
 Doroshenko V., Santangelo A., Ducci L., Klochkov D., 2012, *A&A*, **548**, A19
 Dougherty S. M., Pittard J. M., Kasian L., Coker R. F., Williams P. M., Lloyd H. M., 2003, *A&A*, **409**, 217
 Dubus G., 2013, *A&ARv*, **21**, 64
 Dupree A. K., et al., 1980, *ApJ*, **238**, 969
 El Mellah I., Sundqvist J. O., Keppens R., 2018, *MNRAS*, **475**, 3240
 El Mellah I., Grinberg V., Sundqvist J. O., Driessen F. A., Leutenegger M. A., 2020, *A&A*, **643**, A9
 Eldridge J. J., Tout C. A., 2004, *MNRAS*, **353**, 87
 Erba C., Ignace R., 2022, *ApJ*, **932**, 12
 Falanga M., Bozzo E., Lutovinov A., Bonnet-Bidaud J. M., Fetisova Y., Puls J., 2015, *A&A*, **577**, A130
 Fender R. P., Kuulkers E., 2001, *MNRAS*, **324**, 923
 Fender R. P., Pooley G. G., Durouchoux P., Tilanus R. P. J., Brocksopp C., 2000, *MNRAS*, **312**, 853
 Fenech D. M., et al., 2018, *A&A*, **617**, A137
 Foreman-Mackey D., Hogg D. W., Lang D., Goodman J., 2013, *PASP*, **125**, 306
 Fullerton A. W., Massa D. L., Prinja R. K., 2006, *ApJ*, **637**, 1025
 Gallego-Calvente A. T., et al., 2021, *A&A*, **647**, A110
 Giménez-García A., Torrejón J. M., Eikmann W., Martínez-Núñez S., Oskinova L. M., Rodes-Roca J. J., Bernabéu G., 2015, *A&A*, **576**, A108
 Giménez-García A., et al., 2016, *A&A*, **591**, A26
 Glatzel W., Kiriakidis M., Chernigovskij S., Fricke K. J., 1999, *MNRAS*, **303**, 116
 Goedhart S., et al., 2024, *MNRAS*, **531**, 649
 González-Galán A., 2014, PhD thesis, University of Alacant, Spain
 Gordon Y. A., et al., 2021, *ApJS*, **255**, 30
 Grinberg V., et al., 2015, *A&A*, **576**, A117
 Grunhut J. H., et al., 2017, *MNRAS*, **465**, 2432
 Güdel M., 2002, *ARAA*, **40**, 217
 Gvaramadze V. V., Röser S., Scholz R. D., Schilbach E., 2011, *A&A*, **529**, A14
 Gvaramadze V. V., Alexashov D. B., Katushkina O. A., Kniazev A. Y., 2018, *MNRAS*, **474**, 4421
 Hainich R., et al., 2020, *A&A*, **634**, A49
 Hamann W. R., Koesterke L., 1998, *A&A*, **335**, 1003
 Härer L. K., Reville B., Hinton J., Mohrmann L., Vieu T., 2023, *A&A*, **671**, A4
 Harris C. R., et al., 2020, *Nature*, **585**, 357

⁴ <http://www.astropy.org>

- Haucke M., Cidale L. S., Venero R. O. J., Curé M., Kraus M., Kanaan S., Arcos C., 2018, *A&A*, **614**, A91
- Hubrig S., Sidoli L., Postnov K. A., Schöller M., Kholtygin A. F., Järvinen S. P., 2019, in Oskina L. M., Bozzo E., Bulik T., Gies D. R., eds, IAU Symposium Vol. 346, High-mass X-ray Binaries: Illuminating the Passage from Massive Binaries to Merging Compact Objects. pp 193–196 ([arXiv:1812.04483](#)), doi:10.1017/S1743921318008426
- Kaper L., Henrichs H. F., Nichols J. S., Snoek L. C., Volten H., Zwarthoed G. A. A., 1996, *AAPS*, **116**, 257
- Kaufer A., Stahl O., Prinja R. K., Witherick D., 2006, *A&A*, **447**, 325
- Kraus M., et al., 2015, *A&A*, **581**, A75
- Kretschmar P., et al., 2019, *New Astron. Rev.*, **86**, 101546
- Kretschmar P., et al., 2021, *A&A*, **652**, A95
- Krtićka J., Kubát J., Skalický J., 2012, *ApJ*, **757**, 162
- Lamers H. J. G. L. M., Waters L. B. F. M., 1984, *A&A*, **136**, 37
- Laplace E., Schneider F. R. N., Podsiadlowski P., 2025, *A&A*, **695**, A71
- Lefever K., Puls J., Aerts C., 2007, *A&A*, **463**, 1093
- Lefèvre L., Marchenko S. V., Moffat A. F. J., Acker A., 2009, *A&A*, **507**, 1141
- Leitherer C., Robert C., 1991, *ApJ*, **377**, 629
- Leitherer C., Chapman J. M., Koribalski B., 1995, *ApJ*, **450**, 289
- López-Mirallés J., Peruchó M., Martí J. M., Migliari S., Bosch-Ramon V., 2022, *A&A*, **661**, A117
- Maccarone T. J., Girard T. M., Casetti-Dinescu D. I., 2014, *MNRAS*, **440**, 1626
- Manousakis A., Walter R., 2015, *A&A*, **584**, A25
- Markova N., Puls J., 2008, *A&A*, **478**, 823
- Martínez-Núñez S., Sander A., Gimenez-García A., González-Galán A., Torrejón J. M., González-Fernández C., Hamann W. R., 2015, *A&A*, **578**, A107
- Martínez J. R., del Palacio S., Bosch-Ramon V., 2023, *arXiv e-prints*, p. [arXiv:2310.18669](#)
- Massa D., Prinja R. K., Oskina L. M., 2024, *ApJ*, **971**, 166
- Massi M., Kaufman Bernadó M., 2008, *A&A*, **477**, 1
- McConnell D., et al., 2020, *Publ. Astron. Soc. Australia*, **37**, e048
- McCray R., Kallman T. R., Castor J. I., Olson G. L., 1984, *ApJ*, **282**, 245
- Menchiari S., Morlino G., Amato E., Bucciantini N., Peron G., Sacco G., 2025, *A&A*, **695**, A175
- Miller-Jones J. C. A., et al., 2021, *Science*, **371**, 1046
- Mohamed S., Mackey J., Langer N., 2012, *A&A*, **541**, A1
- Negueruela I., 2019, in Oskina L. M., Bozzo E., Bulik T., Gies D. R., eds, IAU Symposium Vol. 346, High-mass X-ray Binaries: Illuminating the Passage from Massive Binaries to Merging Compact Objects. pp 170–177, doi:10.1017/S1743921319001285
- Negueruela I., Torrejón J. M., Reig P., 2008, in The 7th INTEGRAL Workshop. p. 72, doi:10.22323/1.067.0072
- Nespoli E., Fabregat J., Mennickent R. E., 2008, *A&A*, **486**, 911
- Norris R. P., the EMU Team 2011, *Journal of Astrophysics and Astronomy*, **32**, 599
- Panagia N., Felli M., 1975, *A&A*, **39**, 1
- Parfrey K., Spitkovsky A., Beloborodov A. M., 2016, *ApJ*, **822**, 33
- Peron G., Casanova S., Gabici S., Baghmany V., Aharonian F., 2024, *Nature Astronomy*, **8**, 530
- Pestalozzi M., Torkelson U., Hobbs G., López-Sánchez Á. R., 2009, *A&A*, **506**, L21
- Poveda A., Ruiz J., Allen C., 1967, *Boletín de los Observatorios Tonantzintla y Tacubaya*, **4**, 86
- Pradhan P., Bozzo E., Paul B., 2018, *A&A*, **610**, A50
- Prinja R. K., Howarth I. D., 1986, *ApJS*, **61**, 357
- Puls J., Markova N., Scuderi S., Stanghellini C., Taranova O. G., Burnley A. W., Howarth I. D., 2006, *A&A*, **454**, 625
- Puls J., Vink J. S., Najarro F., 2008, *A&ARv*, **16**, 209
- Ramachandran V., et al., 2025, *A&A*, **698**, A37
- Reig P., 2011, *Ap&SS*, **332**, 1
- Reig P., Chakrabarty D., Coe M. J., Fabregat J., Negueruela I., Prince T. A., Roche P., Steele I. A., 1996, *A&A*, **311**, 879
- Rubio-Díez M. M., Sundqvist J. O., Najarro F., Traficante A., Puls J., Calzoletti L., Figer D., 2022, *A&A*, **658**, A61
- Sadakane K., Hirata R., Jugaku J., Kondo Y., Matsuoka M., Tanaka Y., Hammerschlag-Hensberge G., 1985, *ApJ*, **288**, 284
- Sako M., Liedahl D. A., Kahn S. M., Paerels F., 1999, *ApJ*, **525**, 921
- Sana H., et al., 2012, *Science*, **337**, 444
- Sander A. A. C., Fürst F., Kretschmar P., Oskina L. M., Todt H., Hainich R., Shenar T., Hamann W. R., 2018, *A&A*, **610**, A60
- Sato N., et al., 1986, *PASJ*, **38**, 731
- Sguera V., Romero G. E., Bazzano A., Masetti N., Bird A. J., Bassani L., 2009, *ApJ*, **697**, 1194
- Shakura N., Postnov K., Kochetkova A., Hjalmarsdotter L., 2012, *MNRAS*, **420**, 216
- Shakura N., Postnov K., Sidoli L., Paizis A., 2014a, *MNRAS*, **442**, 2325
- Shakura N., Postnov K., Sidoli L., Paizis A., 2014b, *MNRAS*, **442**, 2325
- Shultz M. E., et al., 2019, *MNRAS*, **490**, 274
- Sidoli L., 2017, in XII Multifrequency Behaviour of High Energy Cosmic Sources Workshop (MULTIF2017). p. 52 ([arXiv:1710.03943](#)), doi:10.22323/1.306.0052
- Staubert R., et al., 2019, *A&A*, **622**, A61
- Sundqvist J. O., Owocki S. P., 2013, *MNRAS*, **428**, 1837
- Sundqvist J. O., Owocki S. P., Puls J., 2018, *A&A*, **611**, A17
- Tejeda E., Toalá J. A., 2025, *ApJ*, **980**, 226
- Torrejón J. M., Negueruela I., Smith D. M., Harrison T. E., 2010a, *A&A*, **510**, A61
- Torrejón J. M., Schulz N. S., Nowak M. A., Kallman T. R., 2010b, *ApJ*, **715**, 947
- Vaughan S., Edelson R., Warwick R. S., Uttley P., 2003, *MNRAS*, **345**, 1271
- Vieu T., Reville B., 2023, *MNRAS*, **519**, 136
- Vink J. S., 2022, *ARAA*, **60**, 203
- Walborn N. R., 1990, in Garmany C. D., ed., *Astronomical Society of the Pacific Conference Series Vol. 7, Properties of Hot Luminous Stars*. pp 23–29
- Watanabe S., et al., 2006, *ApJ*, **651**, 421
- Wilkin F. P., 1996, *ApJL*, **459**, L31
- Wilson W. E., et al., 2011, *MNRAS*, **416**, 832
- Wright A. E., Barlow M. J., 1975, *MNRAS*, **170**, 41
- Yadav A. P., Glatzel W., 2016, *MNRAS*, **457**, 4330
- Zdziarski A. A., 2012, *MNRAS*, **422**, 1750
- Zuo Z., et al., 2025, *arXiv e-prints*, p. [arXiv:2505.23918](#)
- del Palacio S., Bosch-Ramon V., Müller A. L., Romero G. E., 2018, *A&A*, **617**, A13
- del Valle M. V., Romero G. E., 2012, *A&A*, **543**, A56
- van Kerkwijk M. H., van Oijen J. G. J., van den Heuvel E. P. J., 1989, *A&A*, **209**, 173
- van den Eijnden J., Rajwade K., 2024, *Research Notes of the American Astronomical Society*, **8**, 34
- van den Eijnden J., Degenaar N., Russell T. D., Wijnands R., Miller-Jones J. C. A., Sivakoff G. R., Hernández Santisteban J. V., 2018, *Nature*, **562**, 233
- van den Eijnden J., et al., 2021, *MNRAS*, **507**, 3899
- van den Eijnden J., Degenaar N., Russell T. D., Miller-Jones J. C. A., Rouco Escorial A., Wijnands R., Sivakoff G. R., Hernández Santisteban J. V., 2022, *MNRAS*, **516**, 4844
- van den Eijnden J., et al., 2023, *MNRAS*, **526**, L129
- van den Eijnden J., et al., 2024, *MNRAS*, **527**, 4260
- van der Meij V., Guo D., Kaper L., Renzo M., 2021, *A&A*, **655**, A31

APPENDIX A: MM IMAGES

This paper has been typeset from a \LaTeX file prepared by the author.

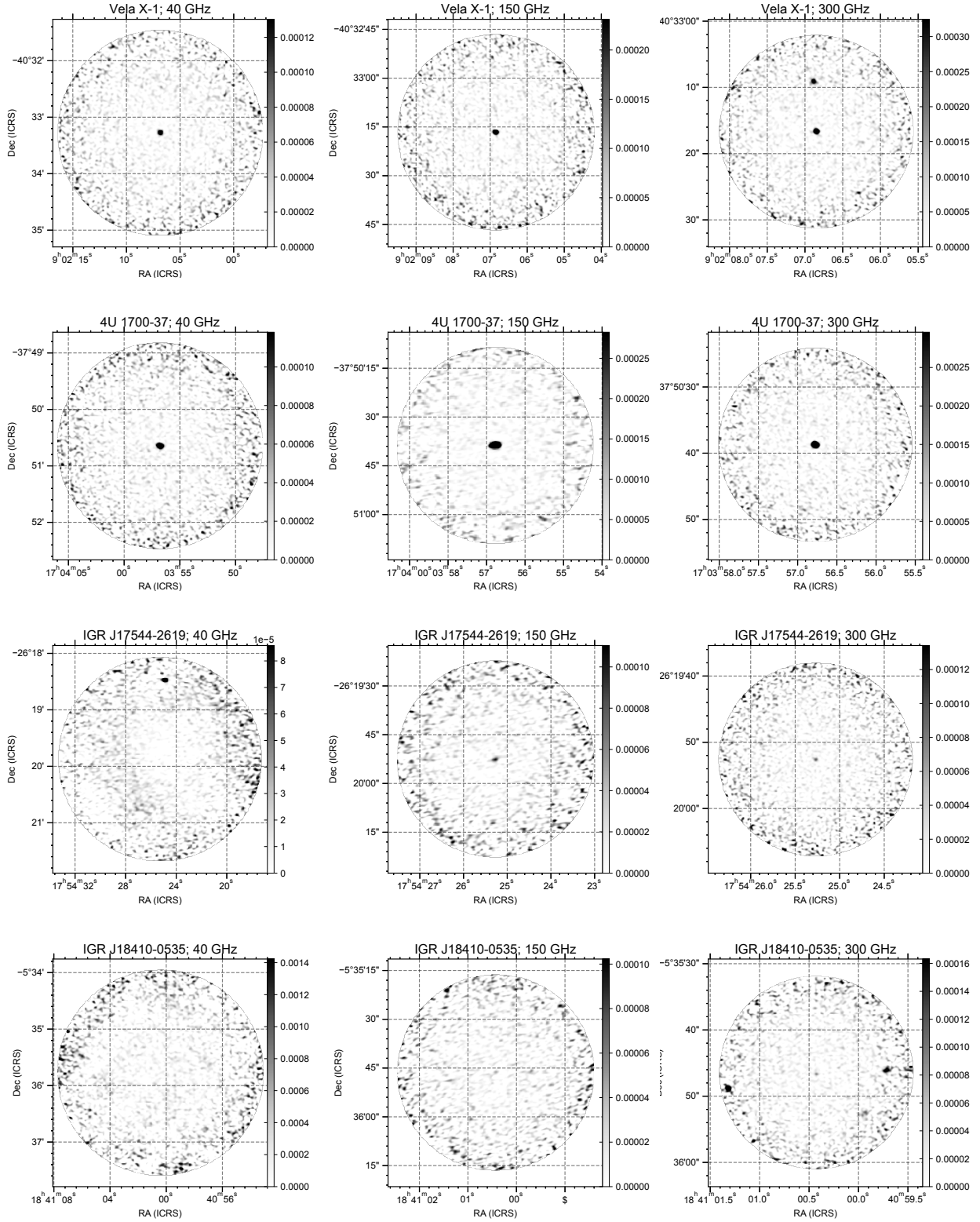


Figure A1. The individual reduced millimeter images of all targets (except 4U 1907+09 at 40/100/150 GHz, shown in the main paper), in each observing band. The target and representative frequency are shown in each subplot's title. Continued in Figure A2.

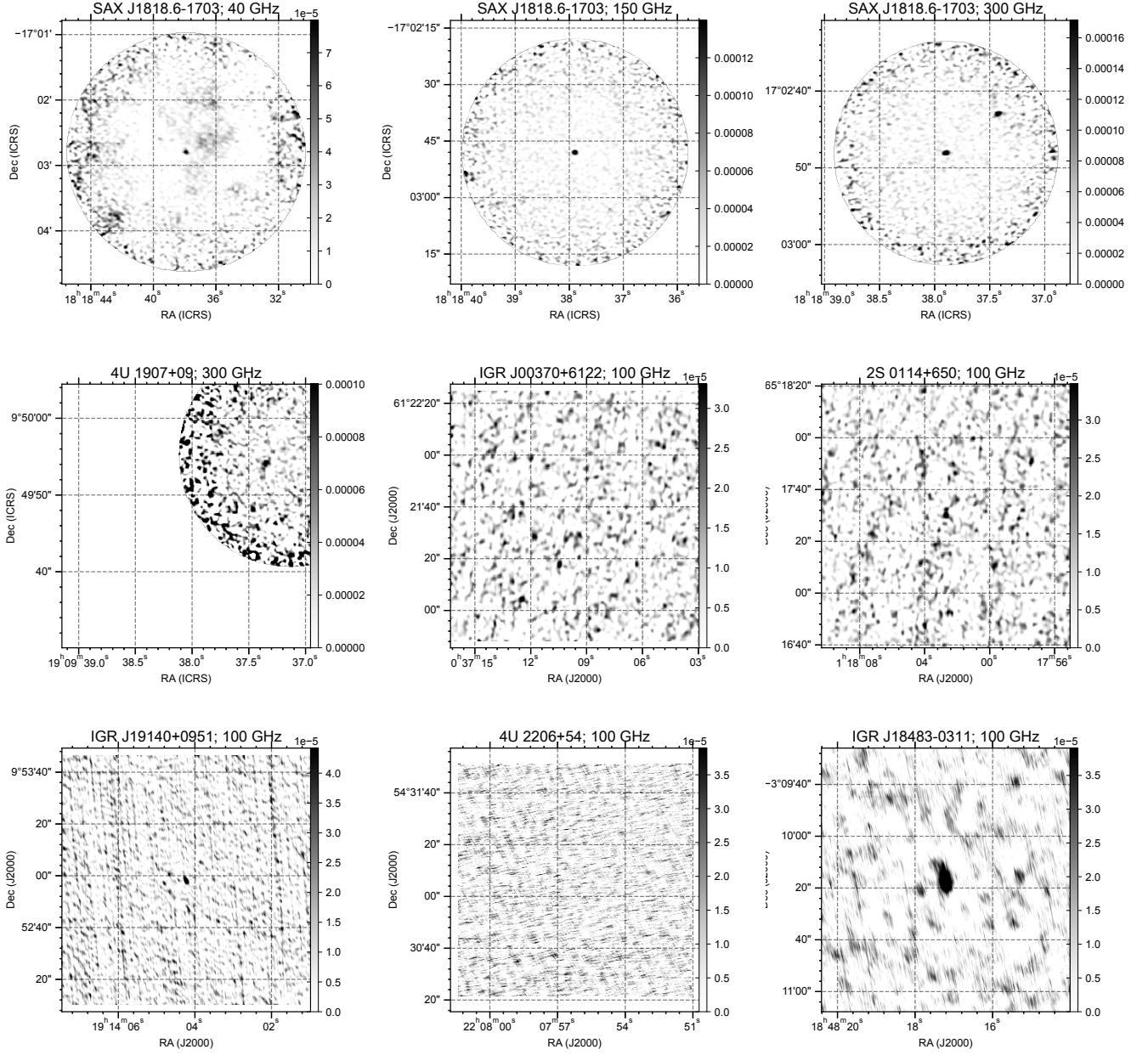


Figure A2. Same as Figure A1.